Numerical simulation of a two-frequency-driven superlattice Faraday-wave pattern

Debashis Panda,[1] Nicolas Périnet,[2] Abdullah M. Abdal,[1,3] Lyes Kahouadji,[1] Seungwon Shin,[4] Jalel Chergui,[1] Damir Juric,[5,6,*] Omar K. Matar,[1,†] and Laurette S. Tuckerman[7,‡]

[1]*Department of Chemical Engineering, Imperial College London, London SW7 2AZ, United Kingdom*
[2]*Departamento de Física, Facultad de Ciencia, Universidad de Santiago de Chile, Santiago, Chile*
[3]*Department of Environmental and Sustainability Engineering, College of Engineering and Energy, Abdullah Al Salem University, 12037 Kuwait City, Kuwait*
[4]*Department of Mechanical and System Design Engineering, Hongik University, Seoul 04066, Republic of Korea*
[5]*Université Paris-Saclay, Centre National de la Recherche Scientifique (CNRS), Laboratoire Interdisciplinaire des Sciences du Numérique (LISN), 91400 Orsay, France*
[6]*Department of Mechanical Engineering, The University of Tokyo, 7-3-1 Hongo, Bunkyo-ku, Tokyo 113-8656, Japan*
[7]*Physique et Mécanique des Milieux Hétérogènes, CNRS, ESPCI Paris, Université PSL, Sorbonne Université, Université Paris Cité, 75005 Paris, France*

The formation of a superlattice pattern in two-frequency-driven Faraday waves discovered and named SSS-I by Arbell & Fineberg (1998, 2002) is investigated by means of Direct Numerical Simulations (DNS) of the full three-dimensional Navier–Stokes equations with a free surface. Two simulations with distinct quasi-hexagonal initial conditions run at a forcing amplitude 25% above the Faraday-wave onset followed quite different routes, but both led eventually to the same superlattice pattern after around 250 forcing periods. This regime is inaccessible to the approximations of weak nonlinearity or viscosity. The standing-wave pattern contain rows of patches, alternating in time between hills and lakes that are connected by a long skeleton resembling the backbone of DNA strands. The patches and skeleton of the pattern can be related to its spatial Fourier decomposition, which combines hexagonal modes with a spatially and temporally subharmonic mode. One of the transition routes passes through several fairly long-lived transients including different hexagonal patterns and another superlattice pattern; the other passes only through erratic and disordered states. After another 100 periods, the pattern became unstable and was succeeded by a dynamic version of SSS-I in which the superlattice is modulated and drifts in the direction of the backbone, while preserving its basic shape. Convergence to SSS-I states both experimentally in a large geometry and numerically from two different initial conditions and in a minimal geometry demonstrates the robustness of the SSS-I pattern.

I. INTRODUCTION

In 2002, Arbell and Fineberg [1] published a major survey of experimental patterns in Faraday waves, the standing waves at the surface of a vertically oscillated fluid layer. This survey was part of the renaissance in the study of Faraday wave patterns that was launched in the mid 1980s by Gollub [2, 3] and Fauve [4, 5] and their colleagues, which was itself part of an explosion of interest in pattern formation that spanned the 1980s to the early 2000s, e.g. [6–10].

In classic fundamental articles, Faraday [11] first described the eponymous waves scientifically in 1831 and Benjamin and Ursell [12] calculated their critical forcing frequency and wavenumber for an inviscid fluid by linear stability analysis in 1954. The Faraday instability is unusual in that its wavelength is determined by the forcing frequency rather than by the depth, facilitating the creation of more varied patterns. The usual patterns are classic: stripes, squares, and hexagons, but more unusual patterns began to be observed experimentally [2, 3], such as supersquares [13] and quasicrystals [14]. This trend accelerated when Edwards & Fauve [15, 16] generalized the Faraday problem from purely trigonometric oscillation to two-frequency forcing in order to excite two spatial scales, thus generating a 12-fold quasipattern.

There followed an avalanche of research on Faraday waves forced by both single and multiple-frequency vibration. Kumar and Tuckerman [17] carried out the first linear stability analysis of the Faraday instability for viscous fluids, followed by Besson *et al.* [18] for two-frequency forcing. Experiments using one [19], two [20] and three [21] frequencies surveyed the parameter dependence of the patterns and revealed new ones, such as triangles [22] and superlattices [23]. Zhang & Viñals [24, 25] derived a quasi-potential equation in the two horizontal coordinates, valid near onset for deep layers of low viscosity, from the three-dimensional Navier-Stokes equations and used it to study pattern selection in the single and two-frequency Faraday configurations. Using the Zhang-Viñals equation, Silber, Skeldon, Porter, and Topaz [26–31] applied the techniques of equivariant bifurcation theory to study the roles played by three-wave interactions, weakly damped modes and the coefficients of the forcing function.

The limitations of the assumptions of weak viscosity and infinite depth were studied by Skeldon and Porter [32] and by Binks *et al.* [33], respectively. Chen and co-workers [34, 35] derived a weakly nonlinear model valid for finite viscosity, which was extended to two-frequency excitation and finite depth [32]. Excellent reviews comparing weakly nonlinear theory to experiment are those of Westra *et al.* [36] for the single-frequency case and Skeldon and Rucklidge [37] for the multiple-frequency case.

These studies have focused primarily on pattern selection at or near the onset of Faraday instability. However, the superlat-

* damir.juric@lisn.fr
† o.matar@imperial.ac.uk
‡ laurette.tuckerman@espci.fr

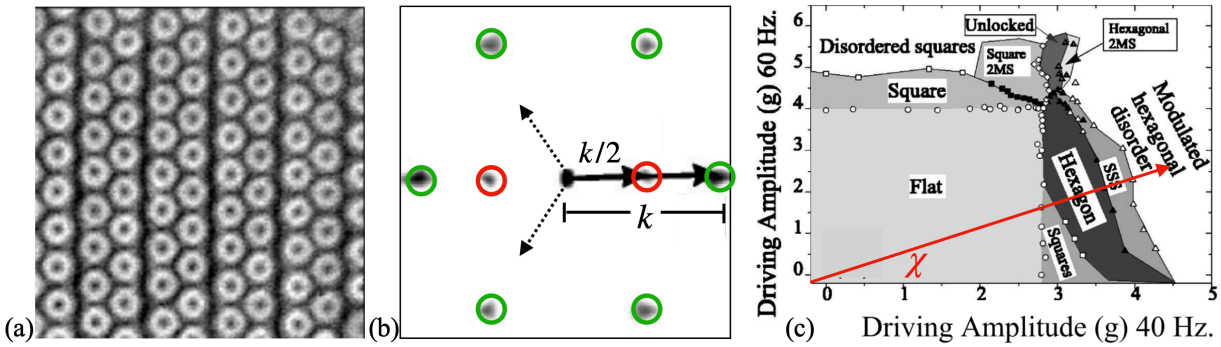

FIG. 1. Experimental SSS-I superlattice pattern, reproduced and adapted with permission from Figures 4 and 5 of Arbell and Fineberg [1]. The density, dynamic viscosity, surface tension, and height of the fluid layer are $\rho_L = 950$ kg/m^3, $\mu_L = 0.0219$ Pa.s, $\sigma = 21.5 \times 10^{-3}$ N/m, $h = 0.155$ cm, respectively, and the imposed vertical oscillation is $F \times [\cos(\chi)\ \cos(2\omega t) + \sin(\chi)\ \cos(3\omega t)]$ with fundamental frequency $\omega = 2\pi(20)$rad s^{-1} and mixing angle $\chi = 30°$. (a) Visualization of height via light intensity. (b) Spatial Fourier transform of (a), showing hexagonal modes (green circles, k) and spatially subharmonic modes (red circles, $k/2$). Sometimes patterns are also observed experimentally that contain one or two other wave-vector pairs, indicated here as dotted arrows. (c) Regime diagram showing which patterns appear with different amplitudes F and proportions dictated by χ of two-frequency forcing with ratio 2:3. The SSS-I state is a secondary bifurcation from hexagons and is observed away from the codimension-two point at which the thresholds corresponding to the frequencies 2ω and 3ω are equal.

tice states we wish to study occur far from the threshold, where weakly nonlinear theoretical approaches are not suitable. Direct Numerical Simulations (DNS) of the Navier-Stokes equations are free from the limitations of weak nonlinearity, as well as any assumptions about depth or viscosity, and can thus be used to study patterns far from onset. We have therefore carried out a long-time quantitative study of the dynamic behaviour of a two-frequency Faraday configuration. We use the successor of a serial code written by Périnet *et al.* [38], who performed the first three-dimensional DNS of Faraday waves using minimal (single-wavelength) square and hexagonal domains for these two basic patterns. This was followed by the numerical discovery by Périnet *et al.* [39] of a complicated and exotic regime alternating between quasi-hexagons and beaded stripes in a minimal hexagonal domain.

Shin *et al.* [40] then wrote a new code, BLUE, based on a hybrid front-tracking/level-set algorithm, which is massively parallelized and thus capable of simulating a much larger domain. Kahouadji *et al.* [41] used this code to carry out the first numerical simulation of a superlattice, a supersquare, in which a large square-wave pattern divides spontaneously into sublattices, a pattern that had been previously observed experimentally by Douady and Fauve [4, 13]. BLUE has since been used to study other related configurations, such as Faraday waves on a sphere [42], sessile drop vibrations [43], drop atomisation [44], and the effect of contaminants on a square-wave pattern [45]. A quite different numerical approach was taken in [46–48], where lubrication theory was used to simulate thin viscous layers subjected to horizontal and vertical vibrations. Richter and Bestehorn [49, 50] utilised this approach to obtain quasipatterns in two-frequency Faraday waves.

Seeking to match the results of [1], Takagi and Matsumoto [51] conducted the first numerical simulations of a two-frequency Faraday configuration using a level-set method. When volume conservation was assured by adding particles near the interface, they obtained the same squares, hexagons, and rhomboids near the onset of instability as [1]. However, they were unable to obtain the superlattice patterns they sought, probably because their computational domain was too small or their simulation was insufficiently long; indeed, the limitations of DNS are those of space and time.

Superlattices, first described for Faraday waves by Kudrolli *et al.* [23], are patterns that have more than one length scale but overall periodicity, in contrast to quasipatterns, which are not spatially periodic [52]. This definition is very broad, and indeed, many types of superlattice patterns have been observed, with either single or two-frequency forcing. Superlattices and quasipatterns can both be formed by combining two hexagonal sets of Fourier modes with the same or different wavenumbers, arranged around a common origin with an angular offset. Indeed, most superlattices in the literature are of this type, particularly the original SL-I and SL-II patterns of [23], the DHS and SSS-II patterns of [1], and those called grid patterns in [53]. Patterns that are not of this category are rhomboids [1, 54], supersquares [13, 41], 2MS [1], and SSS-I [1].

Our article presents a detailed numerical simulation of SSS-I, one of the instances of what Arbell and Fineberg [1] called a Subharmonic Superlattice State because the period of its temporal response is twice that of the two-frequency forcing period. The SSS-I has been studied mathematically by Rucklidge *et al.* [55] and by Matthews [56] using the approach developed by Tse *et al.* [57]. Aside from this, to our knowledge, there have been no other investigations of the SSS-I pattern and certainly no numerical simulations.

The SSS-I is shown in Figure 1, which combines and modifies figures from [1]. Figure 1(a) shows the surface obtained experimentally by light-intensity imaging. The surface consists of white patches traversed and connected by a dark zig-zagging backbone or skeleton, somewhat reminiscent of a strand of DNA. The location of the backbone alternates at each forcing period. Figure 1(b) shows its spatial Fourier spectrum containing three pairs of wavevectors of wavenumber k arranged hexagonally, and another pair of wavenumber $k/2$ which is parallel to one of the pairs of hexagonal wavevectors. Dotted

arrows of length $k/2$ show wavevectors that are present in other versions of SSS-I which will not be studied here. Figure 1(c) shows the regimes obtained in the 2:3 two-frequency-forcing parameter plane and the direction (mixing angle $\chi = 30°$) in the parameter plane that was used both by us and by [1] in seeking SSS-I.

We have found the formation of SSS-I to be a long and complicated process and that obtaining a stable superlattice state from an initial hexagonal state required at least 250 forcing time periods. Moreover, the transition from hexagonal patterns to superlattices is neither unique nor straightforward. In one of our simulations, the transition proceeds via an erratic sequence of disordered states, while in another, it proceeds via intermediate fairly long-lived states, after which it becomes unstable, leading to a new dynamical version of SSS-I in which the pattern is modulated and drifts along the direction of the backbone.

The remainder of this paper is organized as follows. Section II A presents the domain chosen for simulating the SSS-I pattern and the governing equations, while section II B presents the numerical method used for solving the equations. Section II C presents validations in the two-frequency case, by comparisons with the linear thresholds of [18] and with the formation of a hexagonal lattice in [1], while section II D presents the Fourier grid with its relevant modes. Section III A describes the detailed evolution in physical and Fourier space of a simulation carried out at 25% above the Faraday wave threshold that culminates in an SSS-I superlattice. Section III B describes the results of a longer simulation in which this superlattice loses stability to a dynamic SSS-I state. We summarize and discuss our results in Section IV. Appendix A presents some mathematical details about Fourier components symmetry, and Appendix B describes simulations at lower values of the oscillation amplitude.

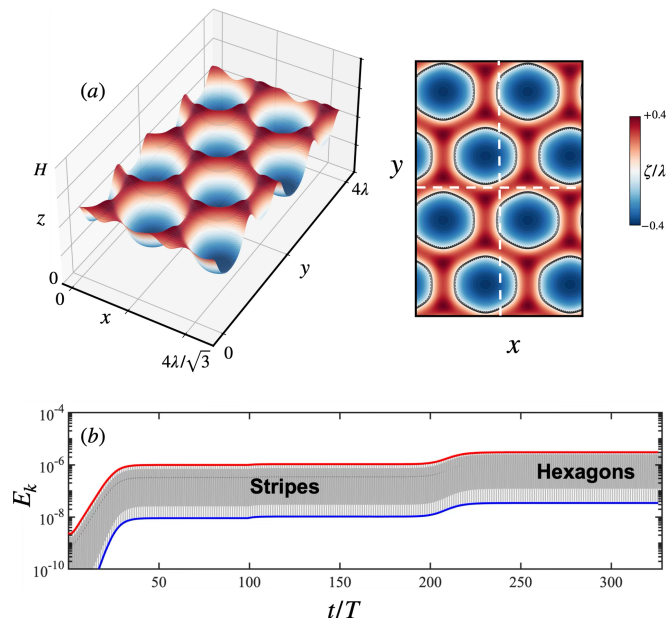

FIG. 2. (a) Instantaneous realisation of a hexagonal pattern in Faraday waves in a cuboidal computational box of dimension $4\lambda_c/\sqrt{3} \times 4\lambda_c \times H$. Left: full three-dimensional domain. Right: two-dimensional projection of interfacial height ζ. The domain used to simulate SSS-I is twice as large in each direction as the minimum domain for accomodating a hexagonal pattern, indicated by white dashed lines. The density and viscosity in the liquid phase (air) below (above) the free surface are ρ_l, μ_l and ρ_a, μ_a. (b) Temporal evolution of the system's kinetic energy. The gray region represents the evolution of kinetic energy, while the red and blue envelopes represent the maximum and minimum kinetic energy over a window of one time period.

II. PROBLEM FORMULATION

A. Domain and governing equations

Our three-dimensional domain, shown in figure 2, is bounded by $z = 0$ and $z = H$, and for our superlattice simulations, has a lateral area $4\lambda_c/\sqrt{3} \times 4\lambda_c$, where λ_c is the critical wavelength at the onset of the Faraday instability, and the ratio of $\sqrt{3}$ between the two sides is required in order to accommodate a hexagonal pattern in a periodic rectangular domain [38]. Note that the lateral directions used here are each twice as long as those used to simulate a simple hexagonal pattern. These dimensions are necessary to accommodate the SSS-I pattern, and we will see in section §III A that even these lengths, while adequate, may be insufficient to capture all effects.

The domain consists of air and liquid phases, both Newtonian, incompressible, and immiscible fluids, with densities ρ_a and ρ_l, and dynamic viscosities μ_a and μ_l, respectively. Initially, the two fluids form horizontal layers separated by an interface with surface tension σ. The height of the lower fluid is h. We impose no-slip and no-penetration boundaries at $z = 0$ and $z = H$, while the boundary conditions at the lateral sides are periodic. We write the equations in a frame of reference that oscillates with the imposed two-frequency acceleration

$$F\left[\cos(\chi)\ \cos(k\omega t) + \sin(\chi)\ \cos(l\omega t + \phi)\right], \qquad (1)$$

where k and l are co-prime integers that each multiply the fundamental frequency ω, χ is the mixing angle that determines the proportions of the two frequencies, and ϕ is the phase angle between the two waves.

The governing equations are given by

$$\nabla \cdot \mathbf{u} = 0, \qquad (2a)$$

$$\rho \frac{\mathrm{D}\mathbf{u}}{\mathrm{D}t} = -\nabla p + \nabla \cdot (2\mu \mathbf{D}) + \int_{A(t)} \sigma\kappa\, \mathbf{n}\, \delta(\mathbf{x} - \mathbf{x}_f)\, dA - \rho g\ \left[1 - F(\cos(\chi)\cos(k\omega t) + \sin(\chi)\cos(l\omega t)\right] \mathbf{e}_z, \qquad (2b)$$

where D is the material derivative, $\mathbf{u}$ represents the velocity, $\mathbf{D} = (\nabla\mathbf{u} + (\nabla\mathbf{u})^{\mathrm{T}})/2$ is the rate-of-deformation tensor, and p denotes the pressure. The interface is defined by the three-dimensional Dirac-delta function $\delta(\mathbf{x} - \mathbf{x}_f)$, where $\mathbf{x}_f = (x, y, \zeta(x, y, t))$ is the interface position at any time t, and $\mathbf{e_z}$ is the unit vector in the vertical direction. The interface has mean curvature κ and unit normal $\mathbf{n}$ (directed upward to

the lighter fluid phase); F is the amplitude of the oscillatory acceleration scaled by the gravitational acceleration g, and A is the surface area defined by the instantaneous position of the interface.

In our one-fluid formulation, the local density and viscosity are given by

$$\rho(\mathbf{x},t) = \rho_a + (\rho_l - \rho_a)\mathcal{H}(\mathbf{x},t), \tag{3a}$$

$$\mu(\mathbf{x},t) = \mu_a + (\mu_l - \mu_a)\mathcal{H}(\mathbf{x},t) \tag{3b}$$

where $\mathcal{H}$ is a smooth Heaviside function, fixed to 1 for the liquid phase and 0 for the air. The required boundary conditions for $\mathcal{H}$ are periodicity on the lateral sides and Neumann conditions at the top and bottom. Mass conservation of incompressible fluids is expressed by $D\rho(\mathbf{x},t)/Dt = 0$, which, from Eq. (3a), leads to $D\mathcal{H}/Dt = 0$. Therefore, the interface is implicitly represented by the Heaviside function and advected by the material motion of the fluids.

B. Numerical Method

The computational domain is discretised using a uniform three-dimensional finite-difference grid. This grid allows a standard staggered Marker-And-Cell (MAC) arrangement [58], where velocity components are stored at the cell faces, while scalar variables, such as pressure, are located at the cell centres. Each grid cell has a dimension $\Delta x \times \Delta y \times \Delta z$. Within this domain, the two fluids are separated by a two dimensional interface, which is discretised by triangular elements.

Once the initial and boundary conditions are specified, the velocity and pressure fields are computed using a projection method. Time integration is performed with a second-order Gear scheme. For spatial discretisation, a second-order scheme is used for scalar variables, while the nonlinear advection terms are handled using an essentially non-oscillatory (ENO) method [59].

The capillary forces (per unit volume) are computed using a hybrid level-set/front-tracking method [60]. The information exchange between the fixed grids and the deformable interface is governed by the immersed boundary method [61]. The interface, represented by the triangular elements, is advected according to $d\mathbf{x}_f/dt = \mathbf{u}(\mathbf{x}_f)$, where $\mathbf{u}(\mathbf{x}_f)$ is the interpolated velocity at the interface position obtained from the fixed grids' cell faces. The integration is performed using a second-order Runge-Kutta method. The adaptive time step is chosen as the minimum of the time scales of the viscous, capillary, interfacial, advective, and vibratory evolution.

The code is parallelised over subdomains each containing 32^3 grid points. The velocity field is solved using a parallel Generalised Minimal Residual (GMRES) method, while the pressure Poisson equation is solved by a parallel multigrid method. Communication between the parallel processes is managed using Message Passing Interface (MPI) routines. More details of the numerical framework can be found in [40, 41, 62].

C. Model assessment: linear theory, rolls, and hexagons

To validate our numerical method, we compare the threshold acceleration to destabilise an interface to that of the two-frequency Floquet linear stability analysis of Besson *et al.* [18]. For this test, the computational domain is $\lambda_c/2 \times 2\lambda_c \times H$, where here H is 8 mm. The mesh resolution is $\Delta x = \Delta y = \lambda/128$, $\Delta z = H/128$. The domain is decomposed into $2\times8\times4$ subdomains of each 32^3 grids, such that the global resolution is $64\times256\times128$ grid points. The lower fluid is silicone oil of density $\rho_l = 950$ kg/m^3, dynamic viscosity $\mu_l = 0.02$ Pa.s, and surface tension, $\sigma = 20.6 \times 10^{-3}$ N/m. and occupies height $h = 3$ mm. The lighter fluid is air of density $\rho_a = 1.206$ kg/m^3 and viscosity $\mu_a = 1.82 \times 10^{-5}$ Pa.s. The imposed two-frequency acceleration (1) has fundamental angular frequency of vibration $\omega = 2\pi \times 11$ rad/s and $k = 4$ and $l = 5$. The phase difference ϕ is 0° and the mixing angle χ is 45°.

To determine the computational threshold acceleration, we ran multiple simulations of acceleration amplitude close to the critical acceleration. One such example is summarised in figure 3(a). First, we set the critical wavelength, $\lambda = 0.6125$ cm ($k = 10.258$ cm^{-1}), and ran cases with $F = 3.3, 3.4$, and 3.5. We then extract the envelope of the maximum kinetic energy over each period. The growth rate γ is evaluated as the slope of the kinetic energy envelope in a semi-log plot. We obtained $\gamma = -0.098, 0.066$, and 0.223 for the acceleration amplitudes $F = 3.3$, 3.4, and 3.5, respectively. Assuming that the growth rate at the onset of instability depends linearly on the control parameter F, we use linear interpolation to $\gamma = 0$ to compute the threshold acceleration. This process is summarised in the inset plot of figure 3(a). The same procedure is used to evaluate the threshold acceleration at three other wavenumbers, as shown in figure 3(b). These observations prove that the numerical simulations are in good agreement with the theory in the linear regime.

Figure 3(b) refers to *harmonic* and *subharmonic* tongues, meaning responses to a forcing function with fundamental frequency ω (period T) which have fundamental frequency ω (period T) and $\omega/2$ (period $2T$). Multiples of the fundamental frequency are also present, but for simplicity, we will refer to the fundamental frequency as the frequency. For the single-frequency Faraday instability, both responses exist, but the most usual and prominent response is subharmonic. For example, the simulations by Périnet *et al.* [38] of a hexagonal pattern show a subharmonic response. A harmonic response is sometimes possible; see, e.g., [63, 64], but it is exceptional.

The two-frequency forcing (1) for figure 3(b) is a superposition of $\cos(4\omega t)$, with weighting coefficient $\cos\chi$, and $\cos(5\omega t)$, with coefficient $\sin\chi$. The usual subharmonic response to forcing frequency 4ω would be 2ω, while the usual subharmonic response to forcing 5ω would be $5\omega/2$. Two-frequency forcing yields a mixture of both responses [18], both of which are seen in Figure 3 for mixing angle $\chi = 45°$. The large tongue shown in red is associated with forcing frequency 4ω and has response 2ω, and the neighburing large tongue in black is associated with forcing frequency 5ω and has response frequency $5\omega/2$. Although the response frequency 2ω is subharmonic in the context of forcing by single-frequency

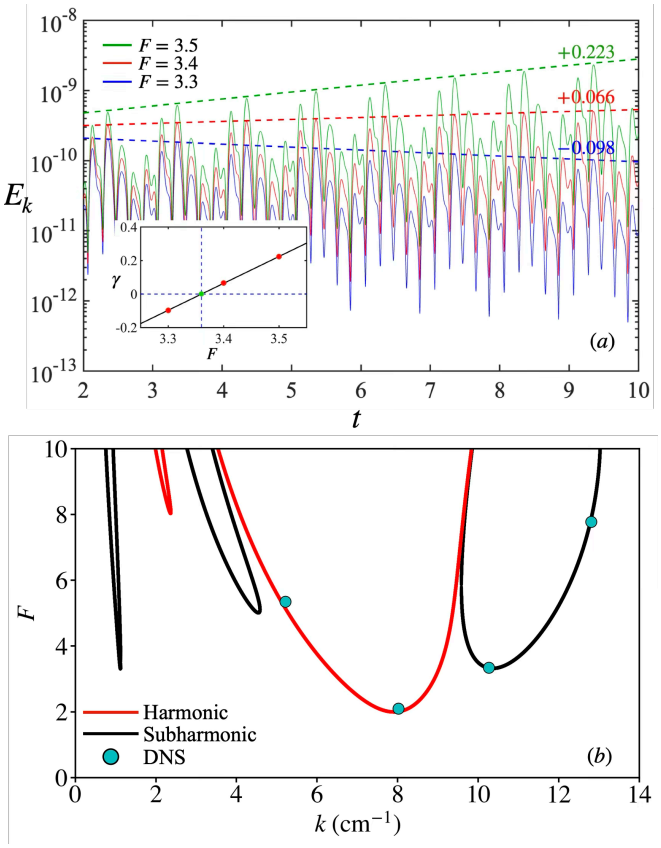

FIG. 3. Validation by comparison with configuration in Besson *et al.* [18]. The physical parameters are $\rho_l = 950$ kg/m^3, $\mu_l = 0.02$ Pa.s, and $\sigma = 20.6\times10^{-3}$ N/m. Forcing parameters are $\omega/2\pi = 11$Hz, $(k,l) = (4,5)$, and $\chi = 45°$. (a) Kinetic energy evolution for $F = 3.3, 3.4$, and 3.5, with the envelope shown as a dashed line. The growth rates for the three values of F are plotted in the inset and a linear interpolation is shown to describe the method of obtaining the threshold acceleration. (b) The DNS results for the thresholds (dots) are compared to the boundaries of the harmonic and subharmonic instability tongues obtained by the linear stability analysis of [18]. The thresholds for the two tongues are equal at the bicritical or codimension-two point, which is $\chi = 60°$ for this configuration.

4ω, it is called *harmonic* in the context of the two-frequency forcing function (1) because it is an integer multiple of the overall frequency ω.

Our main investigation, like that of Arbell and Fineberg [1], has frequencies $(k,l) = (2,3)$ and mixing angle $\chi = 30°$. For this value of χ, the 2ω-frequency forcing, and hence the ω response, is dominant. Given the context of our two-frequency forcing, this response will be called harmonic. We also see temporally subharmonic responses; indeed, the overall temporal dependence of the SSS-I pattern is subharmonic.

This nomenclature also applies to spatial dependence. Given a wavenumber k, nonlinear interactions will necessarily create multiples of k called superharmonics or merely harmonics, merely by the elementary calculation $e^{ikx}e^{ikx} = e^{2ikx}$. When considering wavevectors oriented in different directions, $2k$ must be replaced by vector sums $\mathbf{k_1} + \mathbf{k_2}$. In the superlattice patterns that we investigate, modes with wavenumber $k/2$, which are *spatially subharmonic* to k, are also observed. The mechanisms by which modes with linearly stable wavenumbers are generated and maintained are the topic of the many theoretical works cited in the introduction.

A grid independence test is also carried out for the critical points of the harmonic and subharmonic tongues, as summarised in table I. The threshold acceleration converges as the number of grid points per wavelength increases. For 32 grid points, the error drops to below 1% and the solution converges as we increase the resolution from 64 to 128 with an error of approximately 0.5%. This shows that at least 32 grid points per wavelength are necessary to represent the two-frequency Faraday waves in the linear regime to 1% accuracy.

The next test for grid convergence is carried out in the nonlinear regime. We increase the acceleration above the threshold amplitude. Three mesh sizes are considered, $\lambda/\Delta x = 32, 64$, and 128, for which we set $\lambda = 0.783$ cm and $F = 1.1\times2.118$. The kinetic energy profiles and their envelope are shown in figure 4(a). The linear growth of the kinetic energy eventually saturates due to nonlinear effects. A significant difference is observed during the linear growth regime. However, as time progresses, saturation of the kinetic energy is observed in all three cases. The finer the grid resolution, the more time is taken to reach saturation. Once the envelope reaches the saturated state, an insignificant difference is observed in increasing the resolution, as shown in the inset of figure 4(a).

Snapshots of the x-z slice at $y = \lambda/4$ for $t \in [23T, 24T + T/4]$ for $\lambda/\Delta x = 64$ are shown in figure 4(b), where the velocity streamlines are overlaid on the slices. Qualitatively, we confirm that the standing interfacial waves are harmonic in nature (compare the snapshots at $t = 23T$ and $24T$). The interfacial height at one of the troughs (x_1) and crests (x_2) at $t = 23T$ is tracked for two time periods. This is shown in figure 4(c). We observe that the interfacial height, ζ, at x_1 and x_2, repeats after one time period, confirming that the waves are harmonic in nature. Not only the kinetic energy profile, but also the interfacial heights, $\zeta(x_1)$ and $\zeta(x_2)$, show negligible differences in increasing the grid resolution from 32 to 128. Therefore, a resolution of 32 grid cells per wavelength seems to be adequate at these parameter values for the nonlinear regime as well.

The final validation test uses parameters that match those of the experiments [1]. The density and dynamic viscosity of the silicone oil are set to 950 kg/m^3 and 0.0219 Pa.s. The surface tension is set to 21.5×10^{-3} N/m. The fluid is filled to a height of $h = 0.155$ cm, and the height of the computational domain is $H = 1$ cm. The parameters for the imposed oscillation (1) are the fundamental driving frequency $\omega = 2\pi(20)$rad s^{-1}, the two oscillation frequencies 2ω and 3ω, the mixing angle $\chi = 30°$, and the phase angle $\phi = 0°$. At mixing angle $\chi = 30°$, the 4ω-frequency forcing, and hence the 2ω response, is dominant. For these parameters, the critical wavelength is $\lambda_c = 0.785$ cm, and we set the lateral size of the domain to $4\lambda_c/\sqrt{3}\times4\lambda_c$, as illustrated in figure 2. The acceleration amplitude is set to $F = 3.46$, which we will denote by F_h. At this amplitude, Arbell and Fineberg [1] determined experimentally that the surface organises into hexagonal patterns.

TABLE I. Grid independence test in the linear regime: the method is repeated for two wavenumbers and grid convergence for the threshold amplitude (Comp.) is tested against the theoretical value (Theor.). The error is evaluated as $|F(\text{Theor.}) - F(\text{Comp.})|/F(\text{Theor.}) \times 100\,\%$.

k (cm^{-1})	λ (cm)	No. grid points ($\lambda/\Delta x$)	F (Theor.)	F (Comp.)	Error (%)
10.258	0.6125	128	3.377	3.360	0.503
		64		3.357	0.592
		32		3.352	0.740
		16		3.177	5.922
8.096	0.7830	128	2.118	2.108	0.472
		64		2.102	0.756
		32		2.097	0.992
		16		2.046	3.418

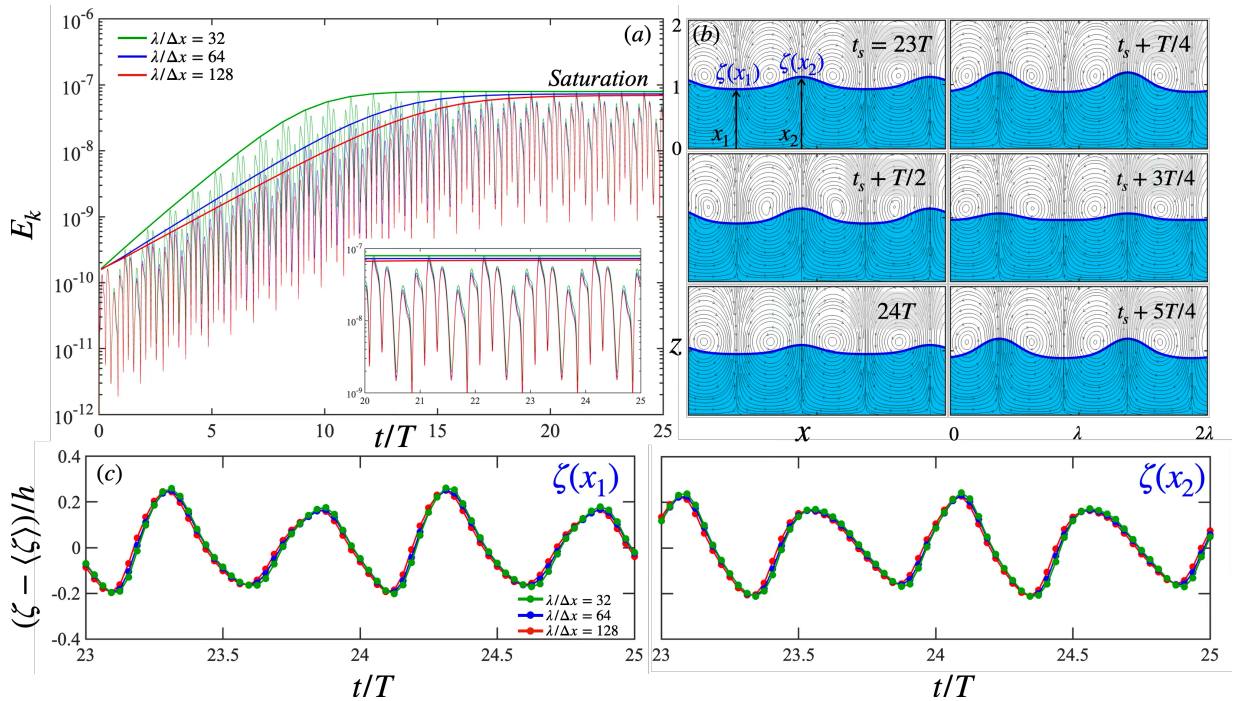

FIG. 4. Grid independence test in the nonlinear regime: (a) Kinetic energy envelope for $F = 2.32$ for 32, 64, and 128 grid points per wavelength. The inset is shown to magnify the evelope and the kinetic energy profile for $t \in [20, 25]$. Temporal evolution of the interface is shown in (b) for $\lambda/\Delta x = 64$, where the blue and white shades represent the liquid and gas phases and is separated by the interface, highlighted as thick deep blue line. The domain is overlaid with velocity streamlines. The temporal evolution of the interface position, ζ at position x_1 and x_2 are shown in (c) for $\lambda/\Delta x = 32, 64$, and 128.

The interface is initialized with stripes as $\zeta = 0.05h\,(\cos k_c y)$, where $k_c = 2\pi/\lambda_c$. After the initial saturation of the stripes, the final state is the hexagonal interface shown in figure 2(a); the temporal evolution of the kinetic energy is shown in figure 2(b). Figure 2(b) also shows that the hexagons persist for at least $100\,T$, during which we observed no secondary instability. This contrasts with [39], for which hexagonal patterns lasted only 10 subharmonic periods before transitioning to more complicated dynamics. Initialising instead with a planar surface perturbed only by numerical error also led to the formation of a stable hexagonal pattern. This leads us to believe that the formation of these hexagonal patterns is independent of the initial state of the system.

D. Fourier space analysis

To quantitatively analyse the pattern, we perform a spatial Fourier analysis of the two-dimensional interfacial elevation $\zeta(\mathbf{x}, t)$, defined by

$$\zeta(\mathbf{x}, jT) = \sum_{m,n} e^{i\mathbf{k}_{mn}\cdot\mathbf{x}} \tilde{\zeta}_{m,n}(jT), \quad j = 0, 1, \ldots \tag{4a}$$

$$\hat{\zeta}_{m,n} = |\tilde{\zeta}_{mn}| \tag{4b}$$

Because the interface $\zeta(x, y)$ is real, the complex amplitude $\tilde{\zeta}_{-m,-n}$ is the complex conjugate of $\zeta_{m,n}$ By a slight abuse of notation, in what follows we will use $\hat{\zeta}_{m,n}$ to designate both the name of the Fourier mode and also its real amplitude. We will retain $\tilde{\zeta}_{m,n}$ to refer to its complex amplitude.

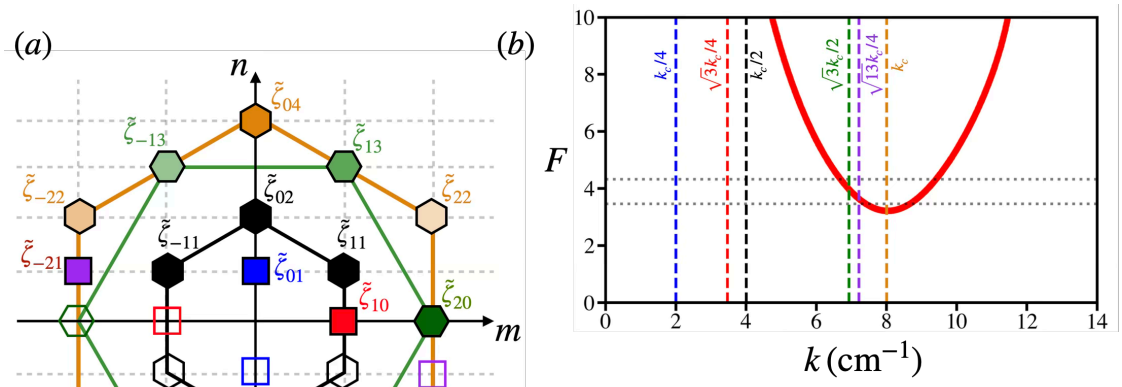

Name	Wavenumber	Indices
Primary hexagonal	k_c	(0,4) (2,2) (−2,2)
Secondary hexagonal	$\sqrt{3}k_c/2$	(2,0) (1,3) (−1,3)
Primary subharmonic	$k_c/2$	(0,2) (1,1) (−1,1)
Secondary subharmonic	$\sqrt{3}k_c/4$	(1,0)
Doubly subharmonic	$k_c/4$	(0,1)
Anomalous	$\sqrt{13}k_c/4$	(−2,0)

FIG. 5. (a) The spatial Fourier space grid with relevant modes. The color coding of the markers will be used thoughout the manuscript. In addition to the *primary hexagonal* modes with critical wavenumber k_c shown in orange, two other hexagons with smaller wavenumbers (larger wavelengths) are present, the *secondary hexagonal* with $k = \sqrt{3}k_c/2$ shown in green, and the *primary subharmonic* ones with $k = k_c/2$ shown in black. Three more *non-hexagonal* modes, shown in red, blue, and purple, play crucial roles in the patterns. These modes have two indices of opposite parity and so cannot be part of a hexagonal triad on our rectangular Fourier grid, as demonstrated in Appendix A 1. (b) Linear instability tongue for the experimental configuration of Arbell and Fineberg [1]. The temporally subharmonic tongue boundary is the thick red curve, inside of which is the linearly unstable regime, i.e. parameter pairs $(k, a/g)$ such that the flat surface vibrated with amplitude a is unstable to perturbations with wavenumber k. Other instability tongues exist, but with minima above $F = 10$. Physical parameters are $\rho_l = 950$ kg/m^3, $\mu_l = 0.0219$ Pa.s, and $\sigma = 21.5 \times 10^{-3}$ N/m. Forcing parameters are $\omega/2\pi = 20$ Hz, $(k, l) = (2, 3)$, and $\chi = 30°$.

The decomposition is carried out over the rectangular computational domain, constraining the admissible wave vectors $\mathbf{k}_{mn}$ to lie on a grid:

$$\mathbf{k}_{m,n} = \left(\sqrt{3}m\,\mathbf{e}_x + n\,\mathbf{e}_y\right) k_c/4, \quad \forall (m,n) \in \mathbb{Z}, \tag{5}$$

where k_c is the critical wavenumber. Thus,

$$|k_{m,n}| = \left(3m^2 + n^2\right)^{1/2} k_c/4. \tag{6}$$

Figure 5(a) shows this grid, as well as the non-negligible Fourier modes governing the dynamic behaviour we have observed in our simulations.

Three sets of modes form hexagons. These modes are shown as hexagonal markers connected by solid lines. The *primary hexagonal modes* $\hat{\zeta}_{-2,2}$, $\hat{\zeta}_{0,4}$, $\hat{\zeta}_{2,2}$ have wavenumber k_c and are shown in orange. The *secondary hexagonal modes*, $\hat{\zeta}_{-1,3}$, $\hat{\zeta}_{1,3}$, $\hat{\zeta}_{2,0}$ have a smaller wavenumber $\sqrt{3}k_c/2$ and are shown in green. Figure 5(b) shows the results of linear stability analysis of the flat interface for the parameters of [1]. In Fig. 5(b), $\chi = 30°$ so, unlike in Fig. 3 for $\chi = 45°$, we are far from the codimension-two point and so the subharmonic tongue (and all other tongues) is above $F = 10$ and so outside of the range of the figure. Vertical dashed lines are drawn at the values of k for which markers are drawn in 5(a), with the same color coding. The primary hexagonal modes are unstable for $F \geq F_h$, while the secondary hexagonal modes become unstable for $F \geq 1.25\,F_h$. The pattern also contains a set of hexagonal modes which have wavenumber $k_c/2$, the *primary subharmonic modes* $\zeta_{0,2}$, $\hat{\zeta}_{1,1}$ and $\hat{\zeta}_{-1,1}$. Shown in black in figure 5(a), these are linearly stable modes of the flat surface.

Three other modes appear with appreciable amplitude in our simulations, all shown as square markers. Mode $\hat{\zeta}_{1,0}$, with wavenumber $\sqrt{3}\,k_c/4$ and shown in red, is subharmonic to the secondary hexagonal modes; we will call it a *secondary subharmonic* mode. Mode $\hat{\zeta}_{0,1}$ with wavenumber $k_c/4$ is shown in blue. It is a subharmonic of the primary subharmonic modes and so we have called it *doubly subharmonic*. Finally, $\hat{\zeta}_{-2,1}$, of wavenumber $\sqrt{13}\,k_c/4$, is shown in purple and will be called *anomalous*. All three of these modes have indices of *mixed parity* so that their sum is odd, i.e. $-2 + 1 = -1$ and $1 + 0 = 1$. Appendix A 1 shows that their images under rotation by $\pi/3$ do not have integer indices and so cannot be represented on the rectangular grid. Such points therefore cannot belong to a hexagon on the grid and we call such modes *non-hexagonal*. Of the three, $\hat{\zeta}_{1,0}$ and $\hat{\zeta}_{0,1}$ fall outside the instability tongue of figure 5(b), while $\hat{\zeta}_{-2,1}$ falls inside.

These three non-hexagonal modes all play important roles, as will be shown in §III. The secondary subharmonic mode $\hat{\zeta}_{1,0}$

is a crucial ingredient of our SSS-I pattern; see Fig. 1(b). The doubly subharmonic mode $\hat{\zeta}_{0,1}$ will be seen in §III C to play an important role in its long-time dynamics. The anomalous mode $\hat{\zeta}_{-2,1}$ plays a prominent, though transient, role in the transition to SSS-I in the simulation of §III A. This mode also appears in a modulated regime found for lower vibrational amplitude, described in Appendix B.

III. SUPERLATTICE STATE

We turn our discussion to the superlattice wave patterns, which arise out of an instability of a hexagonal pattern. We set the forcing amplitude to $F = 1.25\,F_h$ and performed simulations starting from two distinct initial conditions. For the first run, we used the nonlinear hexagonal state at $F = F_h$ as the initial condition. For the second run, we applied random noise to a small-amplitude hexagonal perturbation. In both cases, we obtained the same superlattice pattern but by different routes. We present the results of these two simulations below. We also ran simulations at lower values of the forcing amplitude $F = 1.05\,F_h$ and $F = 1.10\,F_h$, which did not lead to the superlattice pattern. We defer describing these simulations at lower F to the Appendix B.

A. Simulation starting from hexagonal equilibrium at $F = F_h$

We used as the initial condition the hexagonal state obtained in § II C with $F = F_h$ at $t = 350\,T$. The velocity, pressure, and Lagrangian surface fields were saved, the clock was reset to $t = 0$, and the acceleration amplitude was increased to $F = 1.25\,F_h$. The kinetic energy envelope is shown in figure 6(a), and the evolution of the interface heights at different driving periods is shown in figure 6(b). The sudden increase in F leads abruptly to hexagons of higher kinetic energy. The first feature observed is an oscillation of period $2T$ between two very close values of E_k in figure 6(a). Figure 6(b) shows the patterns at $t = 10T$ and $11T$. Both are hexagonal, but they differ slightly. The heights, indicated by the color code, differ between the two instants and at $t = 11T$, a small bump appears at the bottom of the trough and protrusions form on the six edges of the crown surrounding the trough.

Figures 6(c) and 7 show the time evolution of the amplitudes of the significant Fourier modes. The anomalous mode $\hat{\zeta}_{-2,1}$ rises (figure 7(c)) and persists during the erratic phase alongside the broader mode competition. Figure 6(c) represents the mode amplitudes via the size of points on the Fourier grid at various instants, while Figure 7 shows their time evolution as curves grouped by type, with subfigure (a) for the primary hexagonal modes, (b) for the secondary hexagonal modes and the secondary subharmonic mode $\hat{\zeta}_{1,0}$, and (c) for the primary subharmonic hexagonal modes and the anomalous mode $\hat{\zeta}_{-2,1}$.

The short-lived temporally subharmonic hexagonal state can be seen at the beginning of figure 7(a), where the three primary hexagonal modes all oscillate together with period $2T$, with a peak-to-peak amplitude of approximately 20% of their temporal mean. Since all modes surveyed other than those of the primary hexagon are negligible at this time, the changes we see in figure 6(b) between $10T$ and $11T$ must be due to higher spatial harmonics that oscillate subharmonically.

The temporally subharmonic hexagons last until $t \approx 22T$. After this, the kinetic energy envelope, the patterns, and the Fourier spectra all change dramatically, signalling the start of the erratic dynamics. The hexagonal symmetry is lost. In figure 7(a), the amplitude of $\hat{\zeta}_{0,4}$ decreases far below that of the other two primary modes, and its subharmonic $\hat{\zeta}_{0,2}$ in figure 7(c) rises, along with the other two primary subharmonic modes. This is followed by an increase in the secondary hexagonal and the non-hexagonal modes in figures 7(b) and (c). The anomalous mode $\hat{\zeta}_{-2,1}$ rises (figure 7(c)) and persists during the erratic phase alongside the broader mode competition. Recall that the secondary hexagonal modes and $\hat{\zeta}_{-2,1}$ are all linearly unstable modes of the flat surface for $F = 1.25\,f_h$; see figure 5. Between $t = 81\,T$ and $181\,T$, the Fourier spectra show the simultaneous presence of the primary, secondary, and primary subharmonic hexagonal modes, as well as two non-hexagonal modes, giving a total of 11 non-negligible modes, plus their complex conjugates. Eventually, at $t \geq 220\,T$, the simulation converges towards a stationary state in which two of the secondary hexagonal modes $\hat{\zeta}_{\pm 1,3}$ dominate $\hat{\zeta}_{2,0}$, with the secondary harmonic mode $\hat{\zeta}_{1,0}$ between them. All other modes are of negligible amplitude.

This is the spectral composition of the superlattice SSS-I pattern presented by Arbell and Fineberg [1] and reproduced in figure 1, with a crucial modification. The modes present in the SSS-I of [1] are the three *primary* hexagonal modes ($k = k_c$) and one *primary* subharmonic mode ($k = k_c/2$), whereas those in figure 6(c) are the *secondary* hexagonal ($k = \sqrt{3}k_c/2$) and *secondary* subharmonic ($k = \sqrt{3}k_c/4$) modes. We do not know the reason for this difference.

The interface goes through a wide variety of patterns, as shown in the snapshots of figure 6(b). The final superlattice pattern at $250\,T$ features a brown backbone or skeleton centered on $x/\lambda \approx 2$ with period $4/3$ in y/λ, reminiscent of strands of DNA.

We examine the detailed spatiotemporal dynamics of our superlattice pattern in figure 8. We present the temporal evolution of its four Fourier modes over four time periods in figure 8(a). In past representations of the Fourier components, we were concerned with the long-term evolution of the pattern and hence plotted the amplitudes $\hat{\zeta}_{m,n}$ at integer multiples of T. Now, we wish to show the dynamics of the pattern within one or a few periods, and so we plot instead $Z_{m,n} \equiv \hat{\zeta}_{m,n}\ \mathrm{sgn}(\mathrm{Re}(\tilde{\zeta}_{m,n}))$. It can be seen that, while the hexagonal modes have a period of T, the spatially subharmonic mode $\hat{\zeta}_{1,0}$ is also temporally subharmonic, i.e. $2\,T$-periodic, so the overall dynamics is also $2\,T$-periodic. This is also the case in [1] and is indeed the reason for which they chose the name of Subharmonic Superlattice State.

The other panels of figure 8 display visualizations of the interface over $[250\,T, 251\,T]$, with figure 8(c) showing the three-dimensional interface and Figures 8(b,d) showing projections in the vertical plane section S. The interfaces at $t = 250\,T$ and $251\,T$ have the same shape, but are images of one another by a half-wavelength translation in x: the brown "backbone" is at

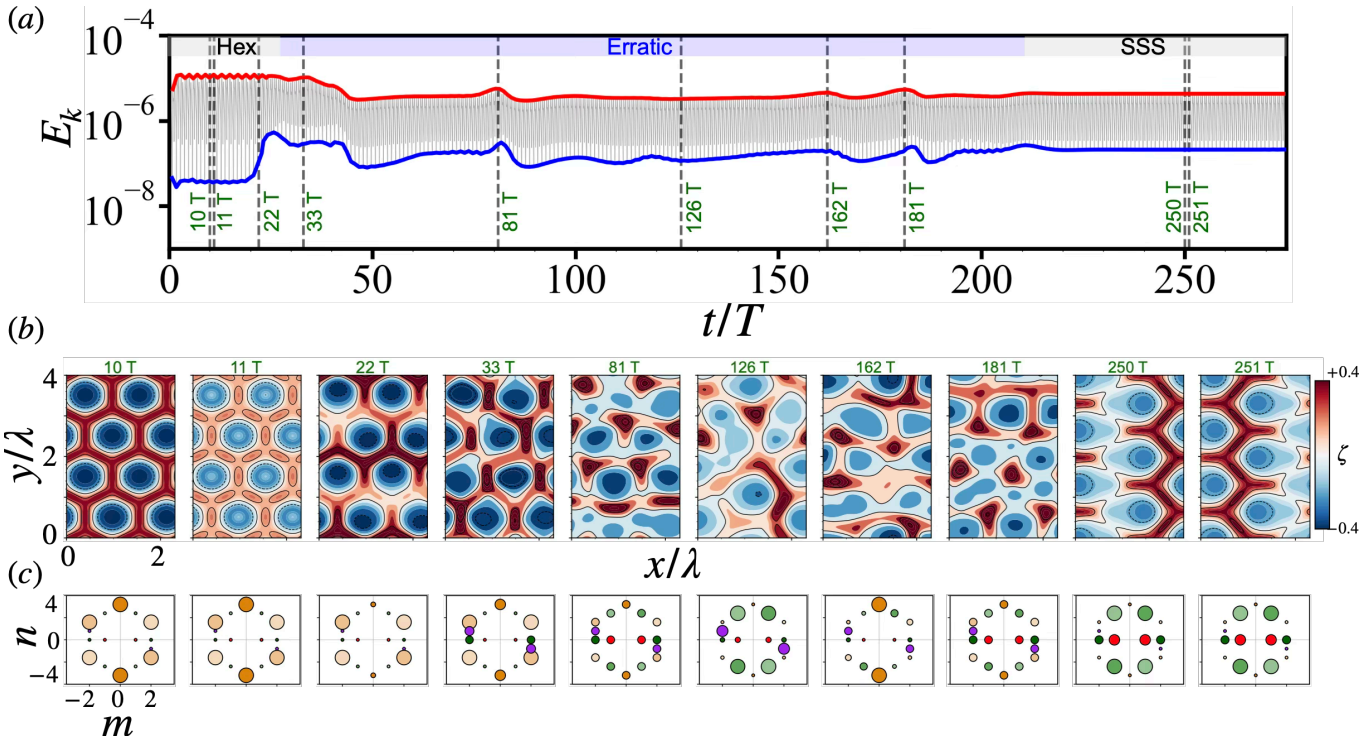

FIG. 6. (a) Envelope of maximum and minimum kinetic energy time series. (b) Interface at instants indicated by dotted lines in E_k profile. (c) Spatial spectra at the same instants, where the color code is that of figure 5, and the size of the markers indicates the mode amplitude. The initial pattern at $10\,T$ consists of primary hexagonal modes (orange). The subharmonic response in the hexagons can be seen by comparing $10\,T$ with $11\,T$. By $126\,T$, secondary hexagonal modes (green) have appeared, and by $250\,T$, the secondary subharmonic mode (red) responsible for the "backbone" is present. The temporally subharmonic (period T) response in the final SSS-I pattern can be seen as the flipping from right to left of the backbone between $250\,T$ and $251\,T$.

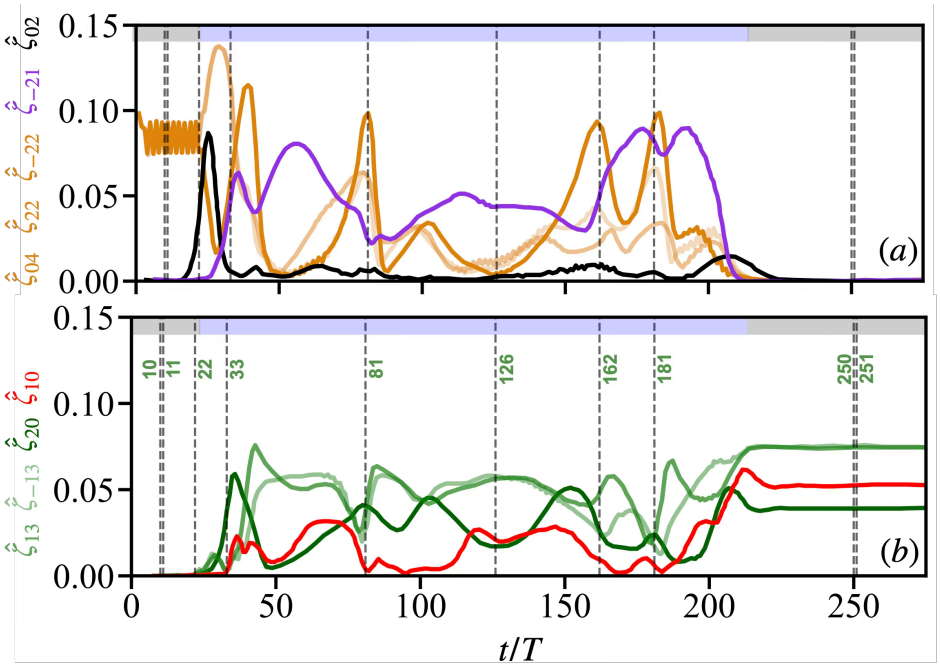

FIG. 7. Temporal evolution of the spatial Fourier coefficients. Curves are color-coded according to the Fourier space grid in figure 5(a). (a) Primary hexagonal (orange) modes comprising initial hexagonal pattern together with primary subharmonic (black, $\hat{\zeta}_{0,2}$) and anomalous modes (purple, $\hat{\zeta}_{-2,1}$). (b) Secondary hexagonal modes (green) together with secondary subharmonic (red, $\hat{\zeta}_{1,0}$) which comprise the SSS-I pattern.

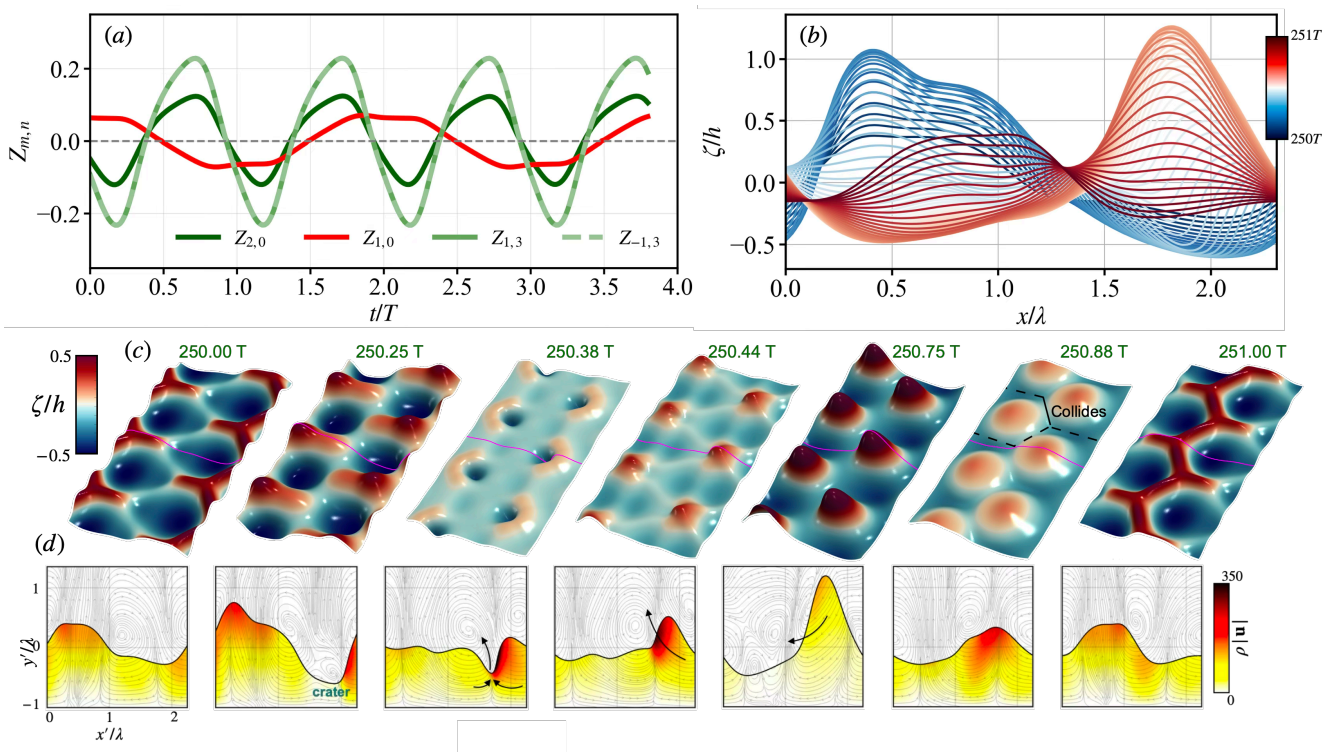

FIG. 8. Temporal behavior of SSS-I pattern. (a) Secondary hexagonal and subharmonic modes comprising the SSS-I pattern over $4T$. Here $Z_{m,n} \equiv \hat{\zeta}_{m,n}\ \mathrm{sgn}(\mathrm{Re}(\tilde{\zeta}_{m,n}))$. The secondary hexagonal modes have period T (temporally harmonic), while the secondary subharmonic mode has period $2T$ (temporally subharmonic). (b,c,d) Temporal behavior over $[250\,T, 251\,T]$. (b) Height of interface along slice S indicated in (c), interface. (d) Two-dimensional projection along S. The difference between the interface at $t = 250$ and $t = 251$ is a manifestation of the fact that $Z_{1,0}(251) = -Z_{1,0}(250)$.

the edges in x at $250\,T$ and at mid-x at $251\,T$. This is due to the contribution by $\hat{\zeta}_{1,0}$ with a temporal period of $2\,T$.

Our simulations have thus produced a superlattice pattern that has the same shape and a Fourier spectrum similar to that of the SSS-I state of Arbell and Fineberg [1], but with some noticeable differences. Their SSS-I pattern is composed of the three primary modes ($k = k_c$) and one primary subharmonic mode ($k = k_c/2$). In contrast, our SSS-I-like pattern contains the three secondary modes ($k = \sqrt{3}k_c/2$) together with $\hat{\zeta}_{1,0}$, which is a spatial subharmonic of the secondary modes ($k = \sqrt{3}k_c/4$). The temporal oscillation of our hexagonal and spatially subharmonic modes is harmonic and subharmonic, respectively, like that of [1].

B. Simulation starting from a perturbed flat interface - long-time behaviour of superlattice wave-patterns

In § III A, we obtained a superlattice wave-pattern and compared it with the SSS-I state obtained by [1]. In this section, we carry out a longer simulation with the same parameters but have chosen a different initial condition: a low-amplitude hexagonal state perturbed with random noise $\eta(x, y)$:

$$\frac{\zeta(x,y)}{h} = 0.05 \sum_{j=0}^{2} \cos\left(k_c\, x \cos\frac{2\pi j}{3} + k_c\, y \sin\frac{2\pi j}{3}\right) + \eta(x,y). \tag{7}$$

We will see that the simulation eventually leads to the same SSS-I state as in section § III A but with a different pathway.

The envelopes of the kinetic energy and the amplitudes of the main Fourier modes are shown in figures 9(a) and 10, respectively. As in section § III A, the kinetic energy seen in figure 9(a) initially rises and saturates at a hexagonal state consisting of primary modes, which we call $\mathrm{Hex_p}$. The state $\mathrm{Hex_p}$ differs from the initial hexagonal state seen in § III A in several ways. First, unlike the temporally subharmonic oscillations (period $2\,T$) observed in § III A, the hexagons here oscillate harmonically (period T) and hence are seen as stationary in figures 9 and 10 over approximately $100\,T$. Second, the kinetic energy of $\mathrm{Hex_p}$ is lower than that of the corresponding state in section § III A. This can be seen by comparing the initial portions of figures 9(a) and 6(a) or those of figures 7(a) and 10.

As was previously the case, the transition from $\mathrm{Hex_p}$ is initiated when the amplitudes of the three primary modes become unequal and the spatial subharmonic $\hat{\zeta}_{0,2}$ rises, here at $t \approx 100\,T$, as seen in figure 10. At later times, the simulations behave quite differently. While the evolution in § III A proceeds via a long erratic phase, here it takes place through a

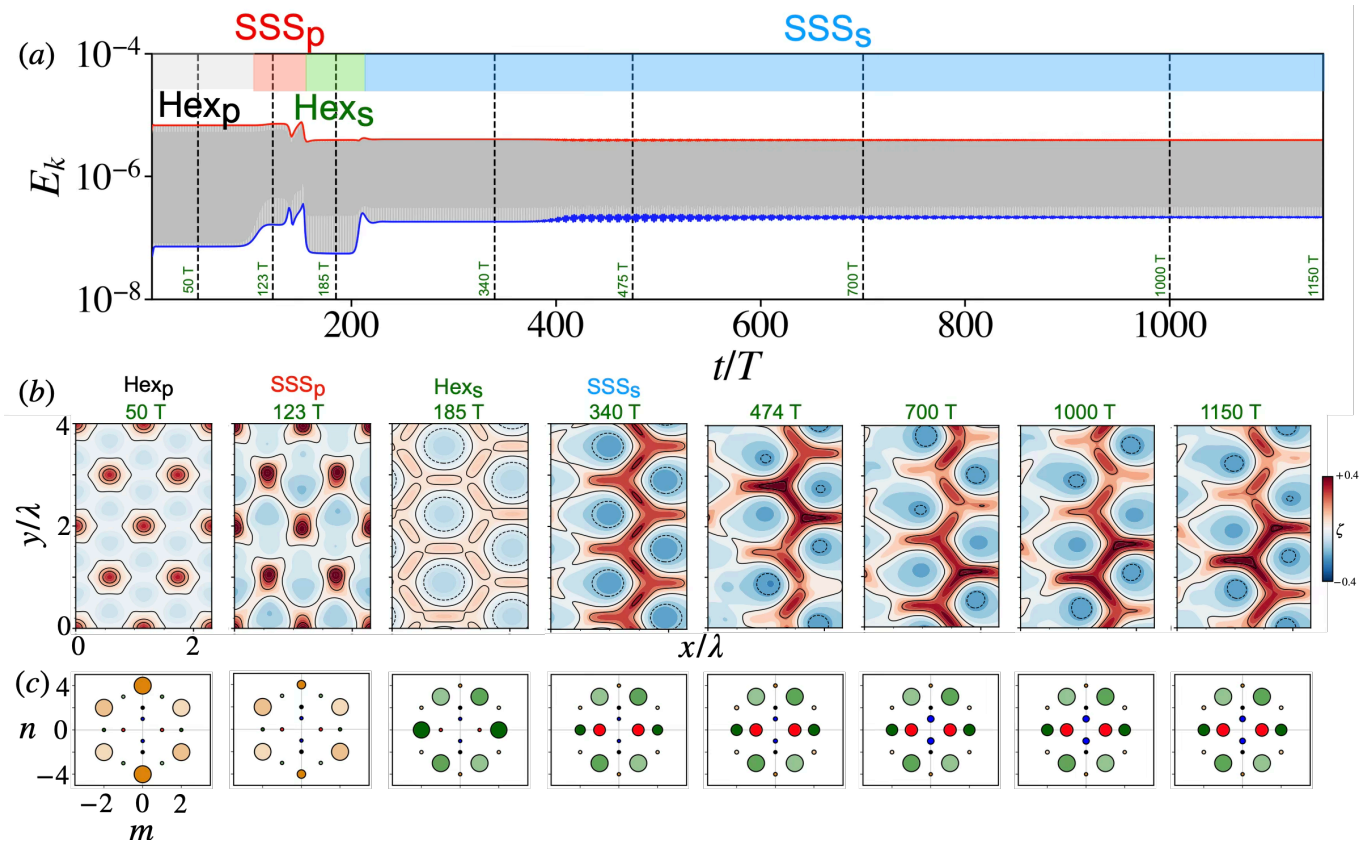

FIG. 9. (a) Envelope of maximum and minimum kinetic energy time series over $t \in [0, 1150\,T]$ for $F = 1.25\,F_h$, starting from initial condition (7). Four sequential regimes are identified and shaded: the primary hexagonal state $\mathrm{Hex_p}$, the primary Subharmonic Superlattice State $\mathrm{SSS_p}$, the secondary hexagonal state $\mathrm{Hex_s}$, and the secondary Subharmonic Superlattice State $\mathrm{SSS_s}$. Vertical dashed lines indicate time instants shown in (b) and (c). (b) Contour plots of the interface height ζ at times indicated above. The first four snapshots are from each of the four regimes, $\mathrm{Hex_p}$, $\mathrm{SSS_p}$, $\mathrm{Hex_s}$, and $\mathrm{SSS_s}$. The four later snapshots show the dynamic SSS state, illustrating a vertical drift of the horizontal arms emanating from the main branch caused by $\hat{\zeta}_{\pm1,3}$ and the modulation in intensity along the backbone driven by $\hat{\zeta}_{0,1}$. (c) Spatial spectra at the same instants, where the color code is that of figure 5, and the size of the markers indicates the mode amplitude. Hex_p contains the primary hexagonal modes (orange), one of which decreases in going to SSS_p. These are succeeded by the secondary hexagonal modes (green) forming Hex_s, one of which diminishes while the secondary subharmonic (red) appears, yielding SSS_s. The remaining spectra correspond to the dynamic SSS and change very little throughout the evolution.

number of quasi-stationary phases, like those manifested when passing through unstable steady states. It is for this reason that we have labelled and named the intermediate phases of this evolution. We call the next state observed a (primary) superlattice state $\mathrm{SSS_p}$ because of its zig-zag appearance and the fact that it consists of the primary hexagonal modes together with a primary subharmonic $\hat{\zeta}_{0,2}$.

Subsequently, a rapid and dramatic change occurs as these primary modes decay and are replaced by the secondary hexagonal modes, which grow to establish a near-hexagonal state $\mathrm{Hex_s}$. (Its slight departure from hexagonal symmetry can be seen by the fact that $\hat{\zeta}_{2,0}$ is slightly lower than the other secondary modes and the hexagonal crowns of 9(b) at $t = 185\,T$ are not perfectly regular.) At $t \approx 200\,T$, the secondary subharmonic mode $\hat{\zeta}_{1,0}$ rises, and by $t \approx 340\,T$, a superlattice has formed that contains the secondary modes together with a spatial subharmonic, which we now call $\mathrm{SSS_s}$. This is the same state as in § III A, more specifically figure 6(b) at $t = 250\,T$.

C. Dynamic SSS-I

Although the simulation appeared to be fairly steady at $\mathrm{SSS_s}$, we continued it to $t = 1150\,T$ to determine its long-term fate. There is no dramatic change in the pattern or in the spectrum after $340\,T$, but figure 9(b) shows that the pattern has shifted along the y direction, and the backbone has become non-uniform. Figure 10 shows the growth and rapid oscillations of certain modes. More specifically, at $t \approx 350\,T$, the doubly subharmonic mode $\hat{\zeta}_{0,1}$ of wavenumber $k_c/4$ appears and develops sustained oscillations. This mode generates the $4\lambda_c$-long modulation in y visible in figure 9(b) for $t \geq 474$. The appearance of $\hat{\zeta}_{0,1}$ also breaks the y-reflection symmetry, as discussed in Appendix A 3. Figure 10 also shows minor changes and oscillations in the modes comprising SSS_s. There is also a resurgence of the primary hexagonal modes, but they remain weak and have little influence on the pattern. These changes all lead to a small but visible modulation of the kinetic

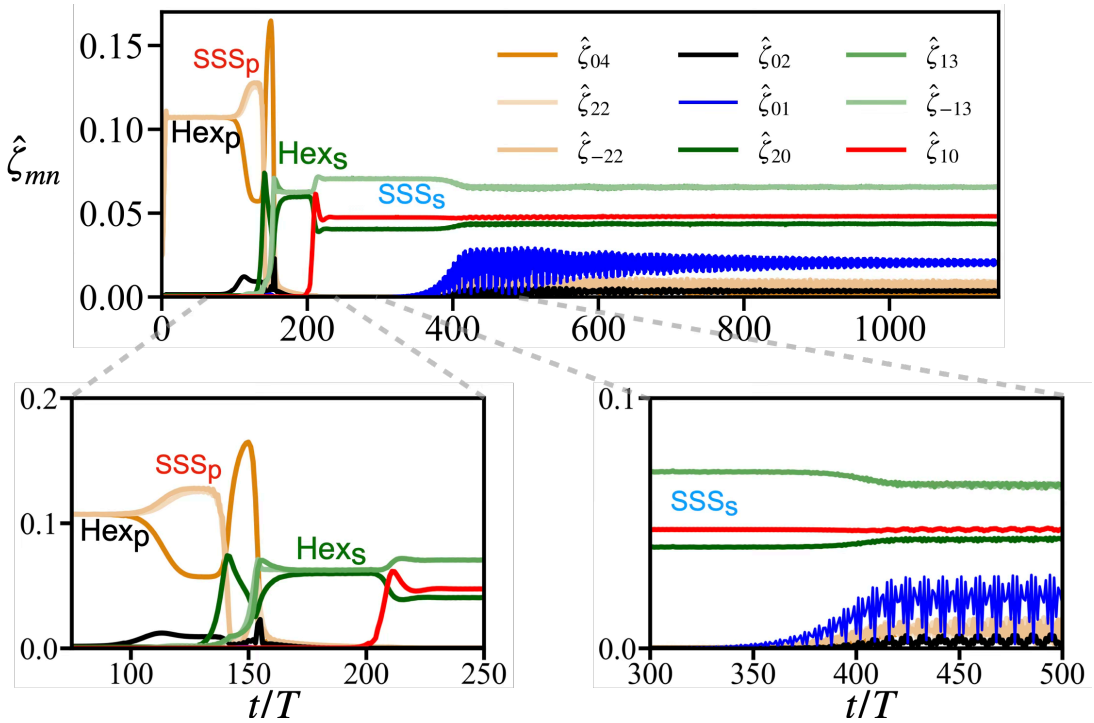

FIG. 10. Temporal evolution of the Fourier mode amplitudes $\hat{\zeta}_{mn}$ for $F = 1.25F_h$. (a) Full interval $t \in [0, 1150T]$: primary modes ($\hat{\zeta}_{0,4}$, $\hat{\zeta}_{2,2}$, $\hat{\zeta}_{-2,2}$), secondary modes ($\hat{\zeta}_{1,3}$, $\hat{\zeta}_{-1,3}$, $\hat{\zeta}_{2,0}$), primary subharmonic mode $\hat{\zeta}_{0,2}$ and non-hexagonal modes $\hat{\zeta}_{1,0}$ and $\hat{\zeta}_{0,1}$. (b) Magnified view of $t \in [0, 205\,T]$ showing the $\mathrm{Hex_p} \to \mathrm{SSS_p} \to \mathrm{Hex_s}$ transition: the three primary modes are equal in $\mathrm{Hex_p}$, $\hat{\zeta}_{0,4}$ rises sharply to form $\mathrm{SSS_p}$, and the secondary modes grow to establish $\mathrm{Hex_s}$. (c) Magnified view of $t \in [250\,T, 600\,T]$ showing the onset at $t \approx 350\,T$ of the dynamic version of the $\mathrm{SSS_s}$ state: the dominant secondary modes and $\hat{\zeta}_{1,0}$ develop slight oscillations, while $\hat{\zeta}_{0,1}$ grows from zero and develops sustained large-amplitude oscillations.

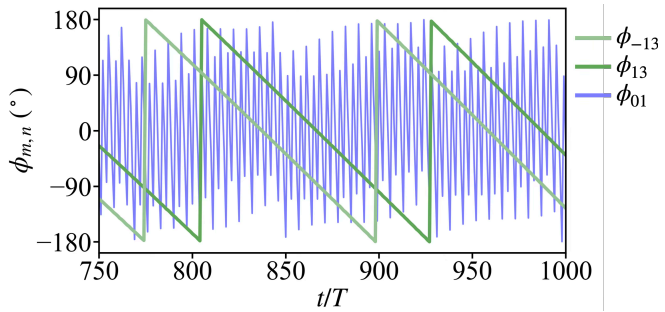

FIG. 11. Temporal evolution of some spatial phases. $\phi_{0,1}$ oscillates rapidly, while $\phi_{1,3}$ and $\phi_{-1,3}$ decrease at the same slow and constant speed.

energy envelope in figure 9(a).

Figure 9(b) for $t \geq 340\,T$ clearly displays the drift of the pattern in the y direction, both in the backbone and in the shifting positions of the crests and troughs. Examination of the phases of the Fourier modes shows that the drift is related to the evolution of the phases $\phi_{1,3}$ and $\phi_{-1,3}$ of the secondary hexagonal modes, shown in figure 11 and discussed in Appendix A 2. These phases change slowly and at a constant rate, completing a cycle of 2π in approximately $120\,T$, after which the branches emanating from the backbone return to their initial locations.

The short-time dependence of the superlattice regime is presented in figure 12. Figure 12(b) shows the evolution of the interface over $8\,T$. (Its most visible feature, already part of the basic SSS pattern and mentioned in § III A, is that the backbone jumps every T from the left half of the box to the right half. This behavior, caused by the subharmonic temporal behavior of the x-dependent mode $\hat{\zeta}_{1,0}$, is seen in figure 8 but not in figure 9(b) because for $t \geq 340\,T$, visualizations are presented only at even multiples of T.) New features of the evolution of the backbones in figure 12(b) are due to the y-dependent mode $\tilde{\zeta}_{0,1}$, which appears only in this dynamic version of SSS_s. The overall intensity of the backbone is governed by the amplitude $\hat{\zeta}_{0,1}$; high-intensity moments like $476\,T$ and $478\,T$ coincide with the maxima in figure 12(a), and low-intensity moments like $477\,T$ coincide with the minima. The position in y of the most intense regions is governed by the phase $\phi_{0,1}$ shown in figure 11. These intense regions travel intermittently along the y axis, staying for $2\,T$ in the lower half of the box and then jumping to the upper half.

The basic SSS-I state consists of four modes with two wavenumbers $\sqrt{3}k_c/2$ and $\sqrt{3}k_c/4$, and two temporal periods, T and $2T$, respectively. Its dynamic version adds to this yet another significant mode, with a different wavenumber $k_c/4$, and three more timescales, all related to the motion of the position and intensity of the backbone. The resulting dynamical SSS-I is a state of great spatio-temporal complexity.

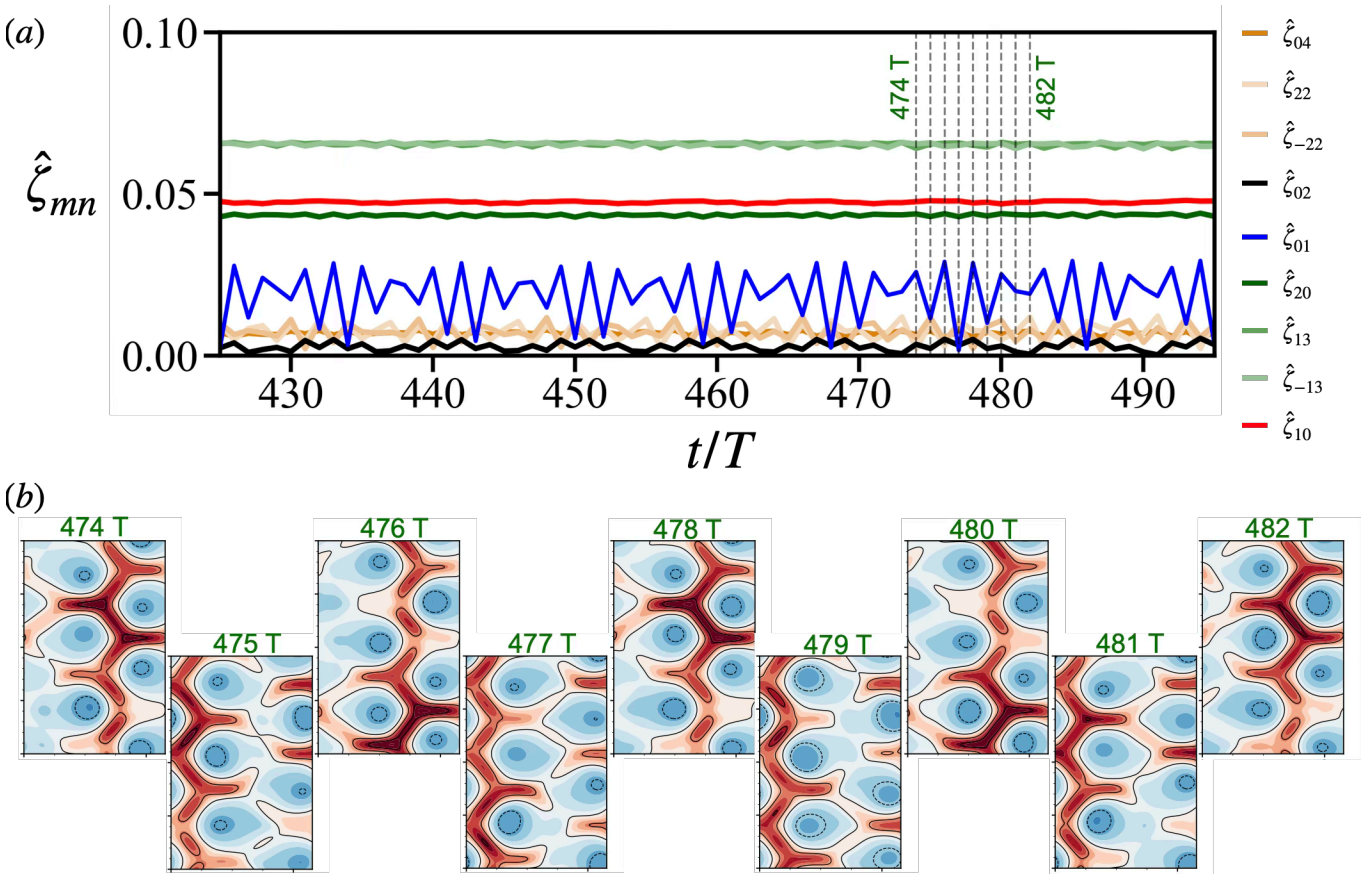

FIG. 12. (a) Magnified view of the Fourier mode amplitudes over $t \in [426T, 495T]$ showing the oscillation of $\hat{\zeta}_{0,1}$ with a period that is between $8\,T$ and $9\,T$. The amplitudes of the other modes are nearly constant. (b) Consecutive interface contour snapshots from $t = 474\,T$ to $482\,T$. The underlying backbone (colored in brown) alternates from left to right at each period T (compare $475\,T$ to $476\,T$), corresponding to the subharmonic temporal behavior of $\hat{\zeta}_{1,0}$. The shift in intensity (dark brown color) along the backbone is related to the spatial phase of the doubly subharmonic mode $\hat{\zeta}_{0,1}$ and has approximate period $4\,T$ (compare $474\,T$ with $478\,T$). The figures span one full modulation cycle.

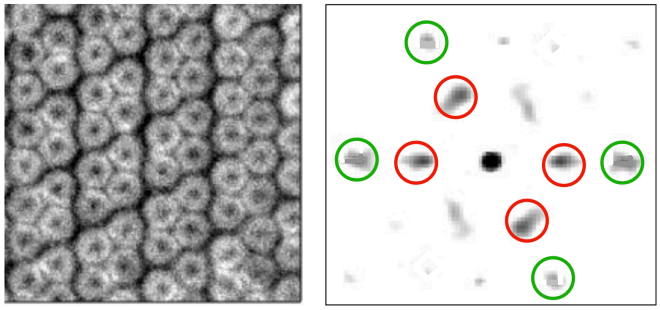

FIG. 13. Experimental SSS-I superlattice pattern, reproduced and adapted with permission from Figure 6 of Arbell and Fineberg [1]. (a) Visualization of height via light intensity. (b) Spatial Fourier transform of (a), showing two hexagonal wave vector pairs (green circles, k) and two spatially subharmonic wave vector pairs (red circles, $k/2$).

IV. CONCLUDING REMARKS

We have numerically simulated a pattern very much like the SSS-I pattern seen experimentally by Arbell and Fineberg [1]. At a forcing amplitude 25% above the Faraday threshold and in a domain whose horizontal dimensions, $4\lambda_c/\sqrt{3} \times 4\lambda_c$ are chosen to accommodate hexagons. We have found a complex time-dependent state that resembles their SSS-I pattern. Its Fourier spectrum is like that illustrated in figure 1: it consists of three secondary hexagonal modes with $k = \sqrt{3}k_c/2$ combined with the secondary subharmonic mode $\hat{\zeta}_{1,0}$ with $k = \sqrt{3}k_c/4$. The resulting interface forms a characteristic zig-zag configuration of crests and troughs with a y-oriented backbone or skeleton.

Moreover, we have obtained the SSS-I pattern via two quite different routes involving many intermediate states and modes. When initiated from the hexagonal state obtained at lower forcing acceleration F_h, the transition proceeds through period doubling followed by an erratic transient involving eleven competing modes before terminating in the final state. In contrast, starting from a randomly perturbed low-amplitude hexagonal interface, a longer simulation leads to a transition through several fairly clearly-defined and long-lived states: the system evolves sequentially from a primary hexagonal pattern $\mathrm{Hex_p}$ to a primary superlattice-like pattern $\mathrm{SSS_p}$, then to a secondary hexagonal state $\mathrm{Hex_s}$, and finally to the secondary

superlattice state SSS_s. SSS_s is eventually succeeded by a dynamic version of this superlattice state, in which the backbone is modulated in intensity and slowly drifts.

For both the basic and dynamic versions of the superlattice states, we have been able to attribute their spatio-temporal features to their non-hexagonal spectral components, most notably the x-dependent $\tilde{\zeta}_{1,0}$ (perpendicular to the backbone) and the y-dependent $\tilde{\zeta}_{0,1}$ (parallel to the backbone). The role of $\tilde{\zeta}_{2,-1}$, which plays a prominent role – transient in Fig. 7, absent in Fig. 10, and permanent in Fig. 19 – remains mysterious.

There are discrepancies between our SSS-I states and those of Arbell and Fineberg [1]. The main difference is that the modes we observe have wavenumbers that differ from theirs by a factor of $\sqrt{3}/2$. We do not know the reason for this. In addition, Arbell and Fineberg [1] observed several variants of their SSS-I pattern involving spatially subharmonic wavevectors in more than one direction, indicated by the dotted arrows that we included in our Fig. 1. Figure 6 of [1], reproduced in modified form in our Fig. 13, shows a pattern with subharmonic wavevectors in two directions, while their Figure 7 shows a state in which there is slow alternation between SSS-I states with subharmonic wavevectors in one, two, and three directions. They are necessarily absent from our simulations because, out of the secondary subharmonic modes ($k = \sqrt{3}k_c/4$) only $\tilde{\zeta}_{\pm 1,0}$ can exist in our computational domain. Other secondary subharmonic modes could, however, fit if we doubled the size of our domain. Alternatively, the full range of SSS-I patterns would fit in our domain if the hexagonal modes of our pattern had remained the primary ones, all of whose subharmonics ($k = k_c/2$) fit in our domain. It would be interesting to see if numerical simulations in a doubled domain would lead to these other versions of SSS-I.

The various versions of SSS-I are also explored and explained in terms of group theory and symmetry by Rucklidge *et al.* [55] and Matthews [56], using temporally discrete (period T) versions of the governing equations. Within this framework, they state that the SSS-I with two subharmonic wave vectors is unstable, while either the version with one or with three subharmonic wave vectors may be stable.

Finally, we mention that SSS-I is only one of the many patterns observed by Arbell and Fineberg [1] for two-frequency-driven Faraday waves. These other patterns may also merit numerical investigations similar to this one.

ACKNOWLEDGEMENTS

This work was supported by the Engineering and Physical Sciences Research Council, UK, through the PREMIERE (EP/T000414/1) programme grant, the ANTENNA Prosperity Partnership grant (EP/V056891/1), and by the National Research Foundation of Korea(NRF) grant funded by the Korea government (MSIT) (No. RS-2025-02302984). O.K.M. acknowledges funding from PETRONAS and the Royal Academy of Engineering for a Research Chair in Multiphase Fluid Dynamics. D.P. and L.K. acknowledge HPC facilities provided by the Imperial College London Research Computing Service. D.P. acknowledges the Imperial College London President's PhD scholarship. D.J. and J.C. acknowledge support through HPC/AI computing time at the Institut du Developpement et des Ressources en Informatique Scientifique (IDRIS) of the Centre National de la Recherche Scientifique (CNRS), coordinated by GENCI (Grand Equipement National de Calcul Intensif) grant 2026 A0202B06721. N.P. acknowledges partial support from FONDECYT Regular through grants 1241498 and 1241542.

DATA AVAILABILITY

The data that support the findings of this article are not publicly available. The data are available from the authors upon reasonable request.

Appendix A: Fourier analysis and symmetry breaking

In what follows, we will discuss the origin of the symmetry breaking of the DNA superlattice due to the presence of the mixed-parity Fourier mode. We first establish the general symmetry condition upon which we will assess the symmetry conditions on the superlattice state. All the results presented here are based on the property of symmetry under an operator γ, which can be a reflection, a rotation, or a translation. If the height of the interface ζ is parameterized by $\mathbf{x} = (x, y)^T$, it is invariant under γ if

$$\zeta(\gamma\mathbf{x}) = \zeta(\mathbf{x}),\ \forall \mathbf{x} \in \mathbb{R}^2. \tag{A1}$$

If we apply (A1) to the Fourier expansion of ζ,

$$\zeta(\mathbf{x}, t) = \sum_{m,n} e^{i\mathbf{k}_{m,n}\cdot\mathbf{x}} \tilde{\zeta}_{m,n}(t), \quad j = 0, 1, \ldots \tag{A2}$$

we can transfer the action of γ successively from $\mathbf{x}$ to $\mathbf{k}_{m,n}$ and then to (m, n) to conclude that (A1) is equivalent to

$$\tilde{\zeta}_{\gamma'(m,n)} = \tilde{\zeta}_{(m,n)},\ \forall (m, n) \in \mathbb{Z}^2. \tag{A3}$$

for some other transformation γ'. From this condition, we extract relations between the modes $\tilde{\zeta}_{m,n}$ of the grid.

1. Hexagonal symmetry in the simulation domain

Here, we establish the conditions for a pattern to have a hexagonal symmetry in a rectangular box whose aspect ratio is $\sqrt{3}$. The simplest way to do so is to pass into the Fourier space. We first recall the elementary symmetries that belong to the hexagonal symmetry group D_6. This group comprises a reflection μ across any diagonal of the hexagon and a rotation of angle $\pi/3$, denoted $\rho_{\pi/3}$, plus all the possible compositions of these isometries; see [10, 65]. For simplicity, we assume the center of rotation to be the origin.

We first wish to determine the constraints on gridpoints (m, n) such that their images under rotation are contained in

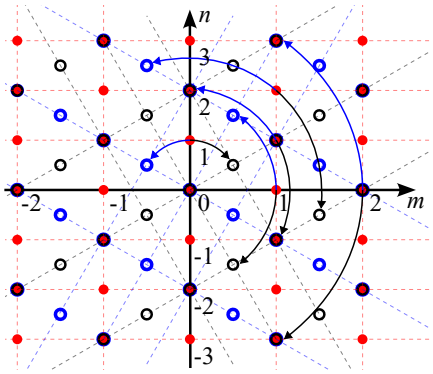

FIG. 14. Grids formed by the $\mathbf{k}_{m,n}$ of the box modes (red disks) and their images by rotations of $\pi/3$ (blue circles) and $-\pi/3$ (black circles). The three grids coincide on points characterized by $m+n$ even where red, black and blue circles are superposed. Only the even modes have images on the red grid, as suggest the few examples of rotation showed by the blue and black bows of circles. Orange arrows represent two base vectors of the coarsest hexagonal network containing the whole red grid.

the grid. Applying the rotation $\rho_{-\pi/3}$ to (m,n) yields:

$$\rho_{-\frac{\pi}{3}}\begin{pmatrix} m \\ n \end{pmatrix} = \begin{pmatrix} (m+n)/2 \\ (-3m+n)/2 \end{pmatrix}. \tag{A4}$$

Definition (A4) provides an example of how a symmetry operator γ on the spatial points (x,y) is used to define γ' on Fourier indices (m,n), as mentioned in (A3). In order for (A4) to be on the grid, $m+n$ and $-3m+n$ must be even, meaning that m and n must be of the same parity. Figure 14 shows that the application of $\rho_{\pi/3}$ sends modes with $m+n$ odd, i..e. with m and n of opposite parity, to images with non-integer indices that do not belong to the rectangular grid. In order for a pattern to have hexagonal symmetry, it is not sufficient for its Fourier coefficients to remain in the grid under rotation by $\pi/3$ and all its multiples, they must also be invariant:

$$\begin{aligned} \tilde{\zeta}_{m,n} &= \tilde{\zeta}_{\frac{m+n}{2},\frac{-3m+n}{2}} = \tilde{\zeta}_{\frac{-m+n}{2},\frac{-3m-n}{2}} = \tilde{\zeta}_{-m,-n} \\ &= \tilde{\zeta}_{\frac{-m-n}{2},\frac{3m-n}{2}} = \tilde{\zeta}_{\frac{m-n}{2},\frac{3m+n}{2}}. \end{aligned} \tag{A5}$$

It follows from (A5) combined with the condition $\tilde{\zeta}_{-m.-n} = \tilde{\zeta}_{m.n}$ that all $\tilde{\zeta}_{m,n}$ are real when the pattern has hexagonal symmetry with center of rotation (0,0). In particular,

$$\phi_{m,n} - \phi_{\frac{m+n}{2},\frac{-3m+n}{2}} + \phi_{\frac{-m+n}{2},\frac{-3m-n}{2}} = 0 \mod (\pi) \tag{A6}$$

where $\phi_{m,n} = \arg(\tilde{\zeta}_{m,n})$ The motivation for writing (A6) in this way is that it also holds in the more general case in which the center of rotation is not at the origin but at a location $\mathbf{x}_0$, so that $\tilde{\zeta}_{m,n}$ are not all real. Equations (A5) and (A6) then apply in a system of coordinates translated by $-\mathbf{x}_0$. After translating (A6) back to the original coordinates, we obtain:

$$\begin{aligned} &\phi_{m,n} - \phi_{\frac{m+n}{2},\frac{-3m+n}{2}} + \phi_{\frac{-m+n}{2},\frac{-3m-n}{2}} \\ &+ \left(\mathbf{k}_{m,n} - \mathbf{k}_{\frac{m+n}{2},\frac{-3m+n}{2}} + \mathbf{k}_{\frac{-m+n}{2},\frac{-3m-n}{2}}\right)\cdot \mathbf{x}_0 = 0. \end{aligned} \tag{A7}$$

The term in parentheses vanishes, so we again obtain (A6). If modes distributed on different hexagons cohabit, the hexagonal symmetry requires that the symmetry axes of the plane waves composing the pattern all intersect at the same point, which fixes all of the $\phi_{m,n}$.

The hexagonal symmetry group also contains reflections. The simplest case is reflection about the horizontal axis $y=0$, so that $\gamma(x,y) = (x,-y)$ and $\gamma'(m,n) = (m,-n)$. A slightly more complicated case is reflection across horizontal axis $y = y_0$. The pattern $\zeta(\mathbf{x})$ is invariant under reflection in $y = y_0$ if

$$\zeta(x,y) = \zeta(x, 2y_0 - y),\ \forall (x,y) \in \mathbb{R}^2. \tag{A8}$$

$$\tilde{\zeta}_{m,n} = \tilde{\zeta}_{m,-n} e^{i2\mathbf{k}_{m,-n}\cdot(0,y_0)^T},\ \forall (m,n) \in \mathbb{Z}^2. \tag{A9}$$

where, as in the case of rotation, the formalism has been modified to include a translation, here $y \to y+y_0$. The equality (A9) between complex quantities can be decomposed into equations for the norms $\hat{\zeta}_{m,n}$ and the phases $\phi_{m,n}$

$$\hat{\zeta}_{m,n} = \hat{\zeta}_{m,-n}, \tag{A10a}$$

$$\phi_{m,n} - \phi_{m,-n} = 2\mathbf{k}_{m,-n}\cdot(0,y_0)^T \mod 2\pi \tag{A10b}$$

Note that (A10b) does not fix an absolute phase for a given mode: if the phases of $\phi_{m,n}$ and $\phi_{m,-n}$ vary together, the pattern can conserve reflection symmetry. The modes $\tilde{\zeta}_{m,0}$ are completely free, because they are homogeneous in y, and hence admit any line $y = y_0$ as a symmetry axis.

When all equations (A5), (A10a) and (A10b) are satisfied, we obtain the hexagons of Fig. 15(a). If the phase condition (A6) is not satisfied, the symmetry group D_6 is replaced by D_3, which is the symmetry group of equilateral triangles, as shown in Fig. 15(b). If the norm condition based on (A5) fails, we can obtain centered rectangles as shown in Fig. 15(c). If the norm condition (A10a) fails, asymmetric hexagons (symmetry group Z_6) as depicted in Fig. 15(d) can be obtained. This pattern is composed of three modes on two distinct hexagons: $\tilde{\zeta}_{4,2}$, $\tilde{\zeta}_{1,7}$ and $\tilde{\zeta}_{-3,5}$ (norms $\hat{\zeta}_{m,n} = 0.5$, phases $\phi_{m,n} = 0$) and $\tilde{\zeta}_{2,0}$, $\tilde{\zeta}_{1,3}$ and $\tilde{\zeta}_{-1,3}$ (norms $\hat{\zeta}_{m,n} = 1$, phases $\phi_{m,n} = \pi$). Within the same hexagon, the norms are all equal and the phase condition is satisfied, but the symmetry axis of the first hexagon is not a horizontal line, which breaks the (horizontal) reflection symmetry. This symmetry is reestablished if the reflection of the first hexagon across the axis $m = 0$ is added, namely the modes $\tilde{\zeta}_{4,-2}$, $\tilde{\zeta}_{3,5}$ and $\tilde{\zeta}_{-1,7}$, all with norms $\hat{\zeta}_{m,n} = 0.5$ and the appropriate phases $\phi_{m,n} = 0$, as has been done to produce Fig. 15(e).

In summary, a pattern has horizontal reflection symmetry if it contains only modes whose indices have the same parity, the norms of the modes are the same within a hexagon, and its phases satisfy (A6). Equations (A10) can be generalized to other directions of reflection axes.

2. Phase condition for horizontal reflection symmetry of a superposition of $\tilde{\zeta}_{2,0}$, $\tilde{\zeta}_{1,3}$ and $\tilde{\zeta}_{-1,3}$

We consider the three hexagonal modes $\tilde{\zeta}_{2,0}$, $\tilde{\zeta}_{1,3}$ and $\tilde{\zeta}_{-1,3}$, associated with the wave vectors $\mathbf{k}_{2,0}$, $\mathbf{k}_{1,3}$ and $\mathbf{k}_{-1,3}$, respectively, where:

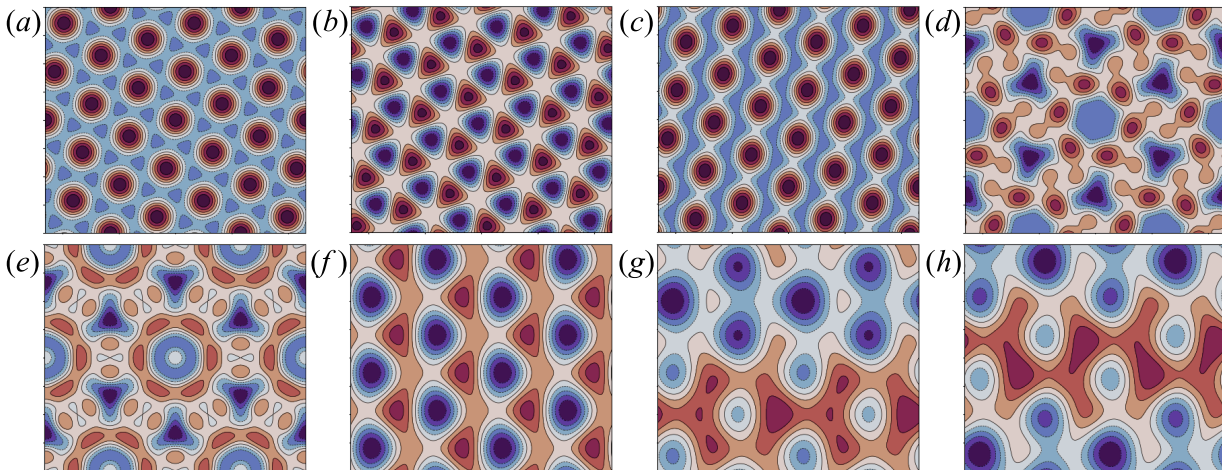

FIG. 15. (a)-(c) Examples of patterns formed by modes $\tilde{\zeta}_{3,-1}$, $\tilde{\zeta}_{2,4}$ and $\tilde{\zeta}_{-1,5}$. (d) pattern formed by two hexagons not aligned angularly: $\tilde{\zeta}_{4,2}$, $\tilde{\zeta}_{1.7}$ and $\tilde{\zeta}_{-3,5}$ and $\tilde{\zeta}_{2,0}$, $\tilde{\zeta}_{1,3}$ amd $\tilde{\zeta}_{-1,3}$. (e) Pattern formed by the same modes as in (e), plus the modes $\tilde{\zeta}_{4,-2}$, $\tilde{\zeta}_{1,-7}$ and $\tilde{\zeta}_{-3,-5}$, which restore the axial symmetry across the axis $y = 0$. (f) Pattern formed by modes $\tilde{\zeta}_{2,0}$, $\tilde{\zeta}_{1,3}$ amd $\tilde{\zeta}_{-1,3}$. (g,h) Examples of patterns formed by modes $\tilde{\zeta}_{2,0}$, $\tilde{\zeta}_{1,3}$, $\tilde{\zeta}_{-1,3}$ and $\tilde{\zeta}_{0,1}$ with and without symmetry across a horizontal axis.

$$\mathbf{k}_{2,0} = \frac{k_c}{4}\left(2\sqrt{3}, 0\right), \mathbf{k}_{1,3} = \frac{k_c}{4}\left(\sqrt{3}, 3\right), \mathbf{k}_{-1,3} = \frac{k_c}{4}\left(-\sqrt{3}, 3\right). \tag{A11}$$

The interface height ζ is composed only of these three modes and their complex conjugates. We seek the condition for the patterns formed by the free surface to be reflection-symmetric about $y = y_0$. In particular, we are interested in the case in which all three modes have the same amplitude. Then, we set:

$$\tilde{\zeta}_{2,0} = Z e^{i\phi_{2,0}},\ \tilde{\zeta}_{1,3} = Z e^{i\phi_{1,3}},\ \tilde{\zeta}_{-1,3} = Z e^{i\phi_{-1,3}}. \tag{A12}$$

We would like to know if there is always such an axis for any triplet $\{\phi_{2,0}, \phi_{1,3}, \phi_{-1,3}\} \in [0, 2\pi]^3$.
A pattern that is reflection-symmetric about $y = y_0$ satisfies (A10). We recall that there is no constraint on $\tilde{\zeta}_{2,0}$ because it is homogeneous in y. Substituting (A11)-(A12) into (A10b) for $(m, n) = (1, 3)$ and replacing $-\phi_{m,-n}$ by $\phi_{-m,n}$ yields:

$$2\pi \frac{y_0}{4\lambda_c} + \frac{\phi_{1,3} + \phi_{-1,3}}{6} = 0 \mod \frac{\pi}{3}. \tag{A13}$$

The relation (A13) establishes the dependence of y_0 on $\phi_{1,3}$ and $\phi_{-1,3}$. As a result, there exists a line $y = y_0$ about which ζ has a reflection symmetry for any pair $\left\{\phi_{1,3}, \phi_{-1,3}\right\}$, provided that $\tilde{\zeta}_{1,3}$ and $\tilde{\zeta}_{-1,3}$ have the same amplitude Z. Since $\tilde{\zeta}_{2,0}$ is homogeneous in y, equation (A13) would remain unchanged if $\phi_{2,0}$ or even the norm $\hat{\zeta}_{2,0}$ were varied. In Fig. 15(f), we have plotted an example of such a pattern, with arbitrary phases. If $\phi_{1,3} + \phi_{-1,3}$ were varied, the horizontal symmetry axis would remain but would be translated vertically.

In conclusion, the temporal variation of $\phi_{-1,3}$ and $\phi_{1,3}$ is not responsible for the breaking of the pattern symmetry across a horizontal axis, but merely translates the axis of symmetry.

3. Modification of the phase condition when $\tilde{\zeta}_{0,1}$ is added

We add to ζ of the previous section the mode $\tilde{\zeta}_{0,1} = Z' e^{i\phi_{0,1}}$ associated with the wave vector $\mathbf{k}_{0,1} = \frac{k_c}{4}(0, 1)$. Now (A10b) generates two conditions that must be satisfied simultaneously:

$$\begin{cases} 2\pi \dfrac{y_0}{4\lambda_c} + \dfrac{\phi_{1,3} + \phi_{-1,3}}{6} = 0 \mod \dfrac{\pi}{3} \\ 2\pi \dfrac{y_0}{4\lambda_c} + \phi_{0,1} = 0 \mod \pi \end{cases} \tag{A14}$$

By combining these two conditions, we deduce that a horizontal symmetry axis exists only when:

$$\frac{\phi_{1,3} + \phi_{-1,3}}{6} - \phi_{0,1} = 0 \mod \frac{\pi}{3} \tag{A15}$$

The equation of the axis is given by either of the two conditions of (A14). Figures 15(g,h) show that some combinations of phases $\left\{\phi_{1,3}, \phi_{-1,3}, \phi_{0,1}\right\}$ break the reflection symmetry in $y = y_0$. In Fig. 15(g), a case satisfying the condition (A15) has been chosen ($\left\{\phi_{1,3}, \phi_{-1,3}, \phi_{0,1}\right\} = \left\{\frac{4\pi}{3}, \frac{5\pi}{3}, \frac{\pi}{2}\right\}$). If, for example, $\phi_{0,1}$ were increased by a multiple of $\pi/3$, we would still observe horizontal reflection symmetry, but about a different y. In Fig. 15(h), $\left\{\phi_{1,3}, \phi_{-1,3}, \phi_{0,1}\right\} = \left\{\frac{4\pi}{3}, \frac{5\pi}{3}, 0\right\}$ does not satisfy (A15), hence ζ no longer has a horizontal reflection symmetry axis.

To conclude, when the mode $\tilde{\zeta}_{0,1}$ is present, not all quadruplets $\left\{\phi_{2,0}, \phi_{1,3}, \phi_{-1,3}, \phi_{0,1}\right\}$ are horizontally reflection-symmetric. The addition of $\tilde{\zeta}_{0,1}$ with an arbitrary phase is likely responsible for the breaking of reflection symmetry observed at time $t = 474\,T$ and thereafter; see section III, Fig. 9(b)). This is illustrated in Fig. 11, which tracks the phases $\phi_{0,1}$, $\phi_{1,3}$, and $\phi_{-1,3}$. As shown in Fig. 11, the phases $\phi_{1,3}$ and $\phi_{-1,3}$ are out of phase by $\pi/2$, while $\phi_{0,1}$ oscillates erratically. This phase misalignment results in a deviation $\Delta\phi$, as depicted in Fig. 11(b).

Appendix B: Pattern evolution for $F_h < F < 1.25\,F_h$

Figures 16 and 17 show the evolution at $F = 1.05\,F_h$ starting from the fully developed hexagons at $F = F_h$. Fig. 16(a,b) show that the hexagonal patttern persists until about $45\,T$, when oscillations appear. The three primary hexagonal mode amplitudes separate from one another while the secondary modes appear, as shown in Fig. 17. The oscillations decay and the final pattern, seen in Fig. 16(b) at $300\,T$, is steady. Fig. 16(b) shows that one prominent tilted axis of reflection symmetry remains, inherited from the hexagonal pattern. The amplitudes of the sets of primary and secondary hexagonal modes in Fig. 16(c) and 17 are equal within each set, so there must be hexagonal asymmetry in the phases, i.e. (A6) is violated.

Figures 18 and 19 show the evolution at $F = 1.10\,F_h$, again from the fully developed hexagons at $F = F_h$. Figure 18(a,b) show that the hexagonal regime is succeeded by an erratic transient. The state at $150\,T$, near the end of the erratic period, looks very similar to the final state for $1.05\,F_h$ at $300\,T$. A regime which is periodic in the energy and principal modes with period $38\,T$ is established at around $250\,T$. Figure 18(c) shows the pattern during one such period, where we can note that the pattern at $345\,T$ is translated in both x and y with respect to that at $307\,T$ and that the states at $312\,T$ and $319\,T$ resemble the beaded stripes observed in [39]. Figures 18(c) and 19 show that the modes involved in the asymptotic periodic state are two of the primary hexagonal modes, one secondary hexagonal mode, and the anomalous mode $\zeta_{-2,1}$ which was large but transient in one of the superlattice cases at $1.25\,F_h$; see Fig. 7. The behavior of the anomalous and the hexagonal modes with smaller amplitudes deviate from exact periodicity.

[1] H. Arbell and J. Fineberg, Pattern formation in two-frequency forced parametric waves, Phys. Rev. E **65**, 036224 (2002).
[2] J. P. Gollub and C. W. Meyer, Symmetry-breaking instabilities on a fluid surface, Physica D **6**, 337 (1983).
[3] S. Ciliberto and J. P. Gollub, Chaotic mode competition in parametrically forced surface waves, J. Fluid Mech. **158**, 381 (1985).
[4] S. Douady and S. Fauve, Pattern selection in Faraday instability, Europhys. Lett. **6**, 221 (1988).
[5] S. Douady, S. Fauve, and O. Thual, Oscillatory phase modulation of parametrically forced surface waves, EPL (Europhysics Letters) **10**, 309 (1989).
[6] M. Golubitsky, I. Stewart, and D. G. Schaeffer, *Singularities and Groups in Bifurcation Theory: Volume II* (Springer, 1988).
[7] J. D. Crawford and E. Knobloch, Symmetry and symmetry-breaking bifurcations in fluid dynamics, Annu. Rev. Fluid Mech. **23**, 341 (1991).
[8] M. C. Cross and P. C. Hohenberg, Pattern formation outside of equilibrium, Rev. Mod. Phys. **65**, 851 (1993).
[9] M. I. Rabinovich, A. B. Ezersky, and P. D. Weidman, *The Dynamics of Patterns* (World Scientific, 2000).
[10] R. B. Hoyle, *Pattern Formation: An Introduction to Methods* (Cambridge University Press, 2006).
[11] M. Faraday, On the forms and states of fluids on vibrating elastic surfaces, Philos. Trans. R. Soc. London **52**, 319 (1831).
[12] T. B. Benjamin and F. J. Ursell, The stability of the plane free surface of a liquid in vertical periodic motion, Proc. R. Soc. London Ser. A **225**, 505 (1954).
[13] S. Douady, Experimental study of the Faraday instability, J. Fluid Mech. **221**, 383 (1990).
[14] B. Christiansen, P. Alstrøm, and M. T. Levinsen, Ordered capillary-wave states: quasicrystals, hexagons, and radial waves, Phys. Rev. Lett. **68**, 2157 (1992).
[15] W. S. Edwards and S. Fauve, Parametrically excited quasicrystalline surface waves, Phys. Rev. E **47**, R788 (1993).
[16] W. S. Edwards and S. Fauve, Patterns and quasi-patterns in the Faraday experiment, J. Fluid Mech. **278**, 123 (1994).
[17] K. Kumar and L. S. Tuckerman, Parametric instability of the interface between two fluids, J. Fluid Mech. **279**, 49 (1994).
[18] T. Besson, W. S. Edwards, and L. S. Tuckerman, Two-frequency parametric excitation of surface waves, Phys. Rev. E **54**, 507 (1996).
[19] D. Binks and W. van de Water, Nonlinear pattern formation of Faraday waves, Phys. Rev. Lett. **78**, 4043 (1997).
[20] H. Arbell and J. Fineberg, Temporally harmonic oscillons in Newtonian fluids, Phys. Rev. Lett. **85**, 756 (2000).
[21] Y. Ding and P. Umbanhowar, Enhanced Faraday pattern stability with three-frequency driving, Phys. Rev. E **73**, 046305 (2006).
[22] H. W. Müller, Periodic triangular patterns in the Faraday experiment, Phys. Rev. Lett. **71**, 3287 (1993).
[23] A. Kudrolli, B. Pier, and J. P. Gollub, Superlattice patterns in surface waves, Physica D **123**, 99 (1998).
[24] W. Zhang and J. Viñals, Pattern formation in weakly damped parametric surface waves, J. Fluid Mech. **336**, 301 (1997).
[25] W. Zhang and J. Vinals, Pattern formation in weakly damped parametric surface waves driven by two frequency components, J. Fluid Mech. **341**, 225 (1997).
[26] M. Silber and A. C. Skeldon, Parametrically excited surface waves: Two-frequency forcing, normal form symmetries, and pattern selection, Phys. Rev. E **59**, 5446 (1999).
[27] M. Silber, C. M. Topaz, and A. C. Skeldon, Two-frequency forced Faraday waves: Weakly damped modes and pattern selection, Physica D **143**, 205 (2000).
[28] J. Porter and M. Silber, Broken symmetries and pattern formation in two-frequency forced Faraday waves, Phys. Rev. Lett. **89**, 084501 (2002).
[29] C. M. Topaz and M. Silber, Resonances and superlattice pattern stabilization in two-frequency forced Faraday waves, Physica D **172**, 1 (2002).
[30] J. Porter and M. Silber, Resonant triad dynamics in weakly damped Faraday waves with two-frequency forcing, Physica D **190**, 93 (2004).
[31] C. M. Topaz, J. Porter, and M. Silber, Multifrequency control of Faraday wave patterns, Phys. Rev. E **70**, 066206 (2004).
[32] A. C. Skeldon and J. Porter, Scaling properties of weakly nonlinear coefficients in the Faraday problem, Phys. Rev. E **84**, 016209 (2011).
[33] D. Binks, M.-T. Westra, and W. van de Water, Effect of depth on the pattern formation of Faraday waves, Phys. Rev. Lett. **79**, 5010 (1997).
[34] P. Chen and J. Vinals, Amplitude equation and pattern selection in Faraday waves, Phys. Rev. E **60**, 559 (1999).
[35] P. Chen, Nonlinear wave dynamics in Faraday instabilities, Phys. Rev. E **65**, 036308 (2002).
[36] M.-T. Westra, D. J. Binks, and W. Van De Water, Patterns of

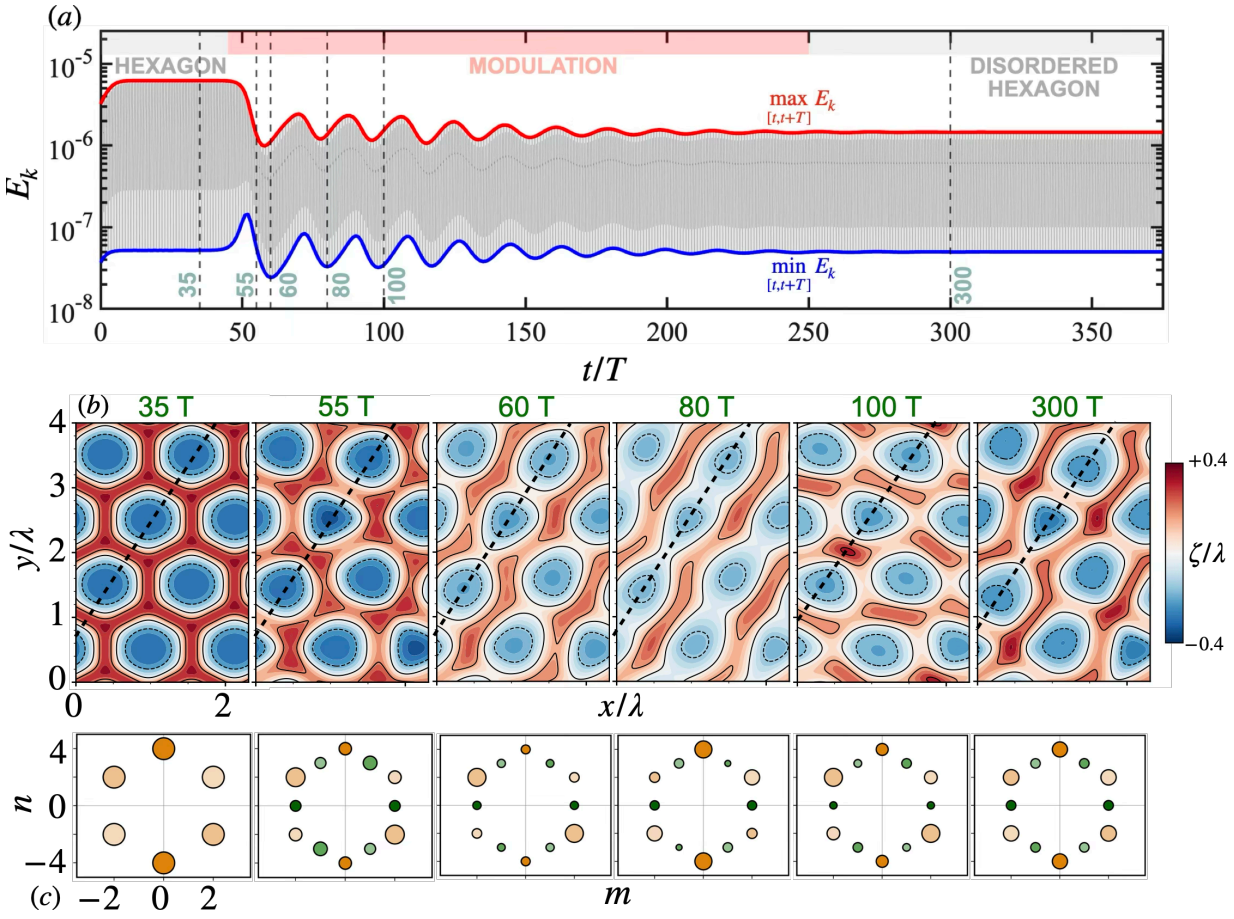

FIG. 16. Pattern evolution for $F = 1.05\,F_h$. (a) The temporal evolution of the kinetic energy, where the red and blue envelopes trace the maximum and minimum kinetic energy over a window averaged over T. The temporal evolution is decomposed into three stages: hexagons, modulation, and disordered hexagons. Dashed lines show axis of reflection symmetry inherited from hexagonal lattice. (b) Contour plots (top) and Fourier spectra (bottom) of the interface height at instants indicated by vertical dotted lines in (a). Color codes of Fourier modes as in Fig. 5. The size of the markers is proportional to their amplitudes.

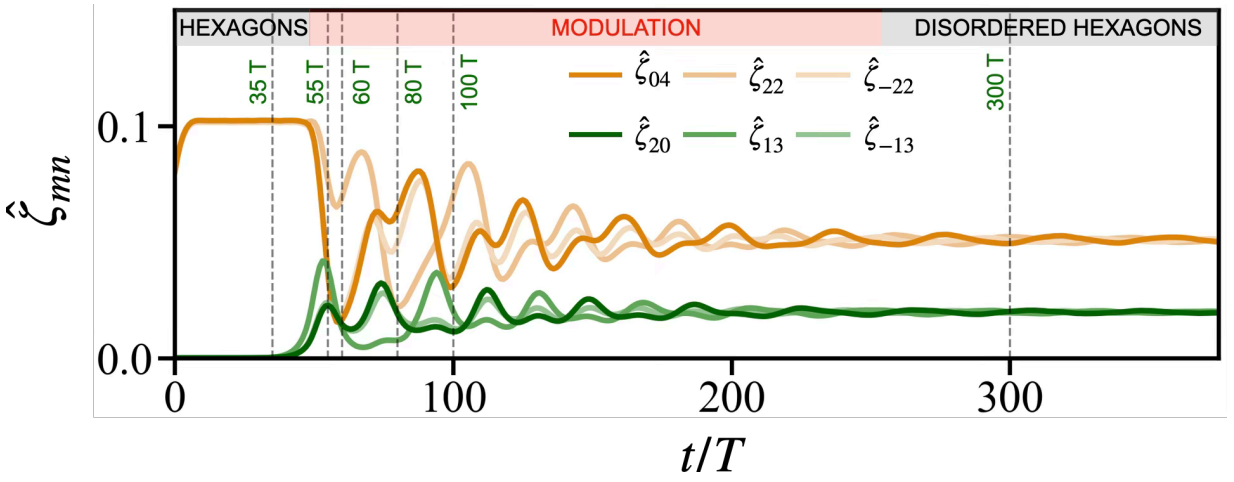

FIG. 17. Temporal evolution for $F = 1.05\,F_h$ of the Fourier mode amplitudes for the primary (orange) and secondary (green) hexagonal modes. The color coding matches that of the Fourier space grid in Fig. 5(a). Vertical dotted lines correspond to the instants shown in Fig. 16.

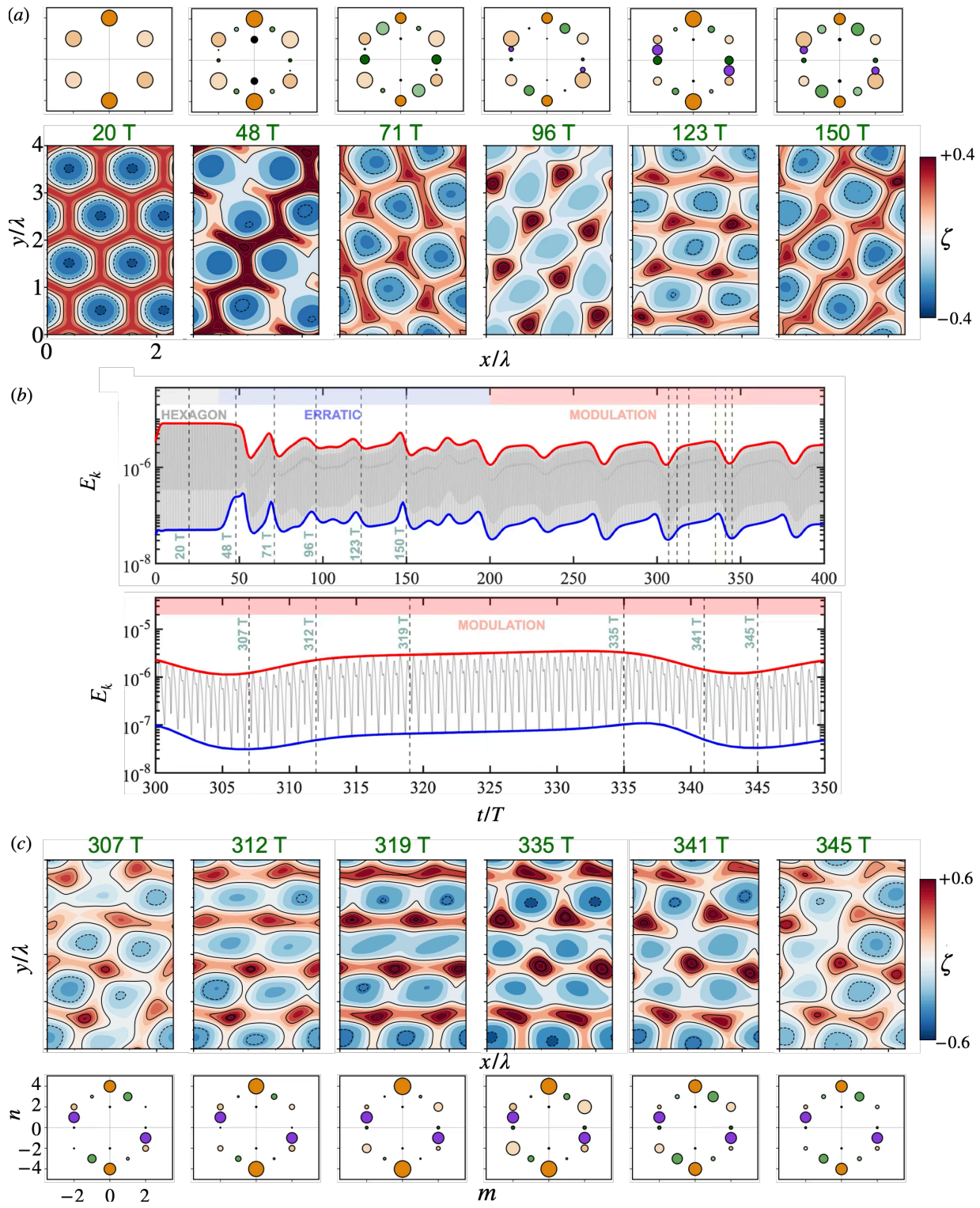

FIG. 18. Pattern evolution for $F = 1.10\,F_h$, divided into three phases: hexagonal, erratic, and modulation. (a) Contour plots of the interface height (top) and Fourier spectra (bottom) over the hexagonal and erratic phases at instants indicated by vertical dotted lines in (b). Temporal evolution of the kinetic energy, with T-averaged envelope of maximum and minimum values over the entire evolution (top) and over a modulation period (bottom). (c) Contour plots of the interface height (top) and Fourier spectra (bottom) over one modulation period at instants indicated by vertical dotted lines in (b). Color codes of Fourier modes as in Fig. 5. The size of the markers is proportional to their amplitudes.

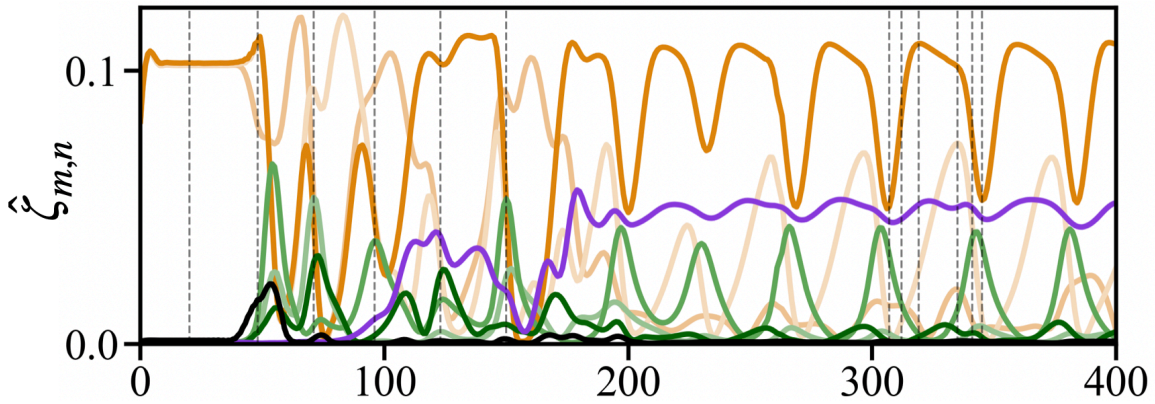

FIG. 19. Temporal evolution for $F = 1.10\,F_h$ of the Fourier mode amplitudes for the primary (orange), secondary hexagonal modes (green), and the anomalous mode $\hat{\zeta}_{-2,1}$ (purple). The color coding matches that of the Fourier space grid in Fig. 5(a). Vertical dotted lines correspond to the instants shown in Fig. 18.

Faraday waves, J. Fluid Mech. **496**, 1 (2003).
[37] A. Skeldon and A. Rucklidge, Can weakly nonlinear theory explain Faraday wave patterns near onset?, J. Fluid Mech. **777**, 604 (2015).
[38] N. Périnet, D. Juric, and L. S. Tuckerman, Numerical simulation of Faraday waves, J. Fluid Mech. **635**, 1 (2009).
[39] N. Périnet, D. Juric, and L. S. Tuckerman, Alternating hexagonal and striped patterns in Faraday surface waves, Phys. Rev. Lett. **109**, 164501 (2012).
[40] S. Shin, J. Chergui, and D. Juric, A solver for massively parallel direct numerical simulation of three-dimensional multiphase flows, J. Mech. Sci. Technol. **31**, 1739 (2017).
[41] L. Kahouadji, N. Périnet, L. S. Tuckerman, S. Shin, J. Chergui, and D. Juric, Numerical simulation of supersquare patterns in Faraday waves, J. Fluid Mech. **772**, R2 (2015).
[42] A. Ebo-Adou, L. S. Tuckerman, S. Shin, J. Chergui, and D. Juric, Faraday instability on a sphere: numerical simulation, J. Fluid Mech. **870**, 433 (2019).
[43] D. Panda, L. Kahouadji, L. S. Tuckerman, S. Shin, J. Chergui, D. Juric, and O. K. Matar, Axisymmetric and azimuthal waves on a vibrated sessile drop, Phys. Rev. Fluids **8**, 110510 (2023).
[44] D. Panda, L. Kahouadji, A. M. Abdal, L. S. Tuckerman, S. Shin, J. Chergui, D. Juric, and O. K. Matar, Drop Medusa: Direct numerical simulations of high-frequency Faraday waves on spherical drops, Phys. Rev. Fluids **9**, 110514 (2024).
[45] D. Panda, L. Kahouadji, L. S. Tuckerman, S. Shin, J. Chergui, D. Juric, and O. K. Matar, Marangoni-driven patterns, ridges and hills in surfactant-covered parametric surface waves, J. Fluid Mech. **1008**, R4 (2025).
[46] N. O. Rojas, M. Argentina, E. Cerda, and E. Tirapegui, Inertial lubrication theory, Phys. Rev. Lett. **104**, 187801 (2010).
[47] M. Bestehorn, Q. Han, and A. Oron, Nonlinear pattern formation in thin liquid films under external vibrations, Phys. Rev. E **88**, 023025 (2013).
[48] S. Richter and M. Bestehorn, Direct numerical simulations of liquid films in two dimensions under horizontal and vertical external vibrations, Phys. Rev. Fluids **4**, 044004 (2019).
[49] S. Richter and M. Bestehorn, Thin-film Faraday patterns in three dimensions, Eur. Phys. J. Spec. Top. **226**, 1253 (2017).
[50] S. Richter, *Direct numerical simulation of nonlinear pattern formation on the surface of liquid films*, Ph.D. thesis, BTU Cottbus-Senftenberg (2021).
[51] K. Takagi and T. Matsumoto, Numerical simulation of Faraday waves oscillated by two-frequency forcing, Phys. Fluids **27** (2015).
[52] S. Fauve and G. Iooss, Quasipatterns versus superlattices resulting from the superposition of two hexagonal patterns, Comptes Rendus. Mécanique **347**, 294 (2019).
[53] T. Epstein and J. Fineberg, Grid states and nonlinear selection in parametrically excited surface waves, Phys. Rev. E **73**, 055302 (2006).
[54] H. Arbell and J. Fineberg, Two-mode rhomboidal states in driven surface waves, Phys. Rev. Lett. **84**, 654 (2000).
[55] A. M. Rucklidge, M. Silber, and J. Fineberg, Secondary instabilities of hexagons: a bifurcation analysis of experimentally observed Faraday wave patterns, in *Bifurcation, Symmetry and Patterns* (Birkhauser, 2003) pp. 101–114.
[56] P. C. Matthews, Automating symmetry-breaking calculations, LMS J. Comput. Math. **7**, 101–119 (2004).
[57] D. P. Tse, A. M. Rucklidge, R. Hoyle, and M. Silber, Spatial period-multiplying instabilities of hexagonal Faraday waves, Physica D **146**, 367 (2000).
[58] F. H. Harlow and J. E. Welch, Numerical calculation of time-dependent viscous incompressible flow of fluid with free surface, Phys. Fluids **8**, 2182 (1965).
[59] M. Sussman, P. Smereka, and S. Osher, A level set approach for computing solutions to incompressible two-phase flow, J. Comput. Phys. **114**, 146 (1994).
[60] S. Shin and D. Juric, A hybrid interface method for three-dimensional multiphase flows based on front tracking and level set techniques, Int. J. Numer. Methods Fluids **60**, 753 (2009).
[61] C. S. Peskin, The immersed boundary method, Acta Numer. **11**, 479 (2002).
[62] S. Shin and D. Juric, Modeling three-dimensional multiphase flow using a level contour reconstruction method for front tracking without connectivity, J. Comput. Phys. **180**, 427 (2002).
[63] K. Kumar, Linear theory of Faraday instability in viscous liquids, Proc. R. Soc. London Ser. A **452**, 1113 (1996).
[64] H. W. Müller, H. Wittmer, C. Wagner, J. Albers, and K. Knorr, Analytic stability theory for Faraday waves and the observation of the harmonic surface response, Phys. Rev. Lett **78**, 2357 (1997).
[65] M. Golubitsky, J. Swift, and E. Knobloch, Symmetries and pattern selection in Rayleigh–Bénard convection, Physica D **10**, 249 (1984).